



# The Detection of a Massive Chain of Dark HI Clouds in the GAMA G23 Field

G. I. G. Józsa<sup>1,2,3</sup> , T. H. Jarrett<sup>4,5</sup> , M. E. Cluver<sup>6,7</sup> , O. I. Wong<sup>8,9</sup> , O. Havenga<sup>4</sup> , H. F. M. Yao<sup>7</sup> , L. Marchetti<sup>4,10</sup> , E. N. Taylor<sup>6</sup> , P. Kamphuis<sup>11</sup> , F. M. Maccagni<sup>12</sup> , A. J. T. Ramaila<sup>3</sup> , P. Serra<sup>12</sup> , O. M. Smirnov<sup>2,3</sup> , S. V. White<sup>2</sup> , V. Kilborn<sup>6</sup> , B. W. Holwerda<sup>13</sup> , A. M. Hopkins<sup>14</sup> , S. Brough<sup>15</sup> , K. A. Pimblet<sup>16</sup> , S. P. Driver<sup>9</sup> , and K. Kuijken<sup>17</sup>

<sup>1</sup>Max-Planck-Institut für Radioastronomie, Radioobservatorium Effelsberg, Max-Planck-Straße 28, D-53902 Bad Münstereifel, Germany;

[gjozsa@mpifr-bonn.mpg.de](mailto:gjozsa@mpifr-bonn.mpg.de)

<sup>2</sup>Department of Physics and Electronics, Rhodes University, PO Box 94, Makhanda, 6140, South Africa

<sup>3</sup>South African Radio Astronomy Observatory, 2 Fir Street, Black River Park, Observatory, Cape Town, 7925, South Africa

<sup>4</sup>Department of Astronomy, University of Cape Town, Private Bag X3, Rondebosch 7701, South Africa; [jarrett@ast.uct.ac.za](mailto:jarrett@ast.uct.ac.za)

<sup>5</sup>Western Sydney University, Locked Bag 1797, Penrith South DC, NSW 1797, Australia

<sup>6</sup>Centre for Astrophysics and Supercomputing, Swinburne University of Technology, John Street, Hawthorn, 3122, Australia; [mcluver@swin.edu.au](mailto:mcluver@swin.edu.au)

<sup>7</sup>Department of Physics and Astronomy, University of the Western Cape, Robert Sobukwe Road, Bellville, 7535, South Africa

<sup>8</sup>CSIRO Space & Astronomy, PO Box 1130, Bentley, WA 6102, Australia

<sup>9</sup>International Centre for Radio Astronomy Research (ICRAR), University of Western Australia, Crawley, WA 6009, Australia

<sup>10</sup>INAF - Istituto di Radioastronomia, Via Gobetti 101, I-40129 Bologna, Italy

<sup>11</sup>Ruhr University Bochum, Faculty of Physics and Astronomy, Astronomical Institute, D-44780 Bochum, Germany

<sup>12</sup>INAF-Osservatorio Astronomico di Cagliari, Via della Scienza 5, I-09047 Selargius (CA), Italy

<sup>13</sup>Department of Physics and Astronomy, University of Louisville, 102 Natural Science Building, Louisville, KY 40292, USA

<sup>14</sup>Australian Astronomical Optics, Macquarie University, 105 Delhi Road, North Ryde, NSW 2113, Australia

<sup>15</sup>School of Physics, University of New South Wales, NSW 2052, Australia

<sup>16</sup>E.A. Milne Centre for Astrophysics, University of Hull, Cottingham Road, Kingston-upon-Hull, Hull HU6 7RX, UK

<sup>17</sup>Leiden Observatory, Leiden University, PO Box 9513, 2300RA Leiden, The Netherlands

Received 2021 October 8; revised 2021 December 2; accepted 2021 December 3; published 2022 February 22

## Abstract

We report on the detection of a large, extended HI cloud complex in the Galaxy and Mass Survey G23 field, located at a redshift of  $z \sim 0.03$ , observed as part of the MeerKAT Habitat of Galaxies Survey campaign (a pilot survey to explore the mosaicing capabilities of the MeerKAT telescope). The cloud complex, with a total mass of  $10^{10.6} M_{\odot}$ , lies in proximity to a large galaxy group with  $M_{\text{dyn}} \sim 10^{13.5} M_{\odot}$ . We identify seven HI peak concentrations, interconnected as a tenuous *chain* structure, extending  $\sim 400$  kpc from east to west, with the largest (central) concentration containing  $10^{9.7} M_{\odot}$  in HI gas distributed across 50 kpc. The main source is not detected in ultraviolet, optical, or infrared imaging. The implied gas mass-to-light ratio ( $M_{\text{HI}}/L_{\text{r}}$ ) is extreme ( $>1000$ ) even in comparison to other *dark clouds*. The complex has very little kinematic structure ( $110 \text{ km s}^{-1}$ ), making it difficult to identify cloud rotation. Assuming pressure support, the total mass of the central concentration is  $>10^{10.2} M_{\odot}$ , while a lower limit to the dynamical mass in the case of full rotational support is  $10^{10.4} M_{\odot}$ . If the central concentration is a stable structure, it has to contain some amount of unseen matter, but potentially less than is observed for a typical galaxy. It is, however, not clear whether the structure has any gravitationally stable concentrations. We report a faint UV-optical-infrared source in proximity to one of the smaller concentrations in the gas complex, leading to a possible stellar association. The system nature and origins is enigmatic, potentially being the result of an interaction with or within the galaxy group it appears to be associated with.

*Unified Astronomy Thesaurus concepts:* Intergalactic medium (813); Intergalactic clouds (809); Interstellar medium (847); Galaxies (573); Galaxy groups (597)

## 1. Introduction

Some of the earliest radio observations already proved the existence of extragalactic neutral hydrogen in the form of intragroup gas or streams in nearby galaxy pairs or groups (Roberts 1968; Weliachew 1969; Roberts 1972; Shostak 1974; van der Hulst 1979a, 1979b; Appleton et al. 1981), the earliest being the Magellanic stream (Hindman et al. 1963a, 1963b; Roberts 1968; Wannier & Wrixon 1972; Mathewson et al. 1974, 1975; Haynes & Roberts 1979). Such gaseous streams were identified as tidal features (Toomre & Toomre 1972; Davies & Wright 1977; Haynes et al. 1979; Sancisi et al. 1984; Yun et al. 1994; Hibbard & Mihos 1995; Barnes &

Hernquist 1996; Putman et al. 1998b). They are not self-gravitating or otherwise dynamically stable, and cannot exist in isolation.

In addition, it soon became clear that intergalactic HI at the current level of column density sensitivity is generally a rarity. In a blind survey with the NRAO 91 cm transit telescope, Shostak (1977) were able to identify one local cloud with negative velocity, likely associated with the Magellanic Stream. Lo & Sargent (1979), in an HI survey of three galaxy groups, were not able to detect isolated clouds, but identified (four) new dwarf systems instead.

Generally, despite counter-indications (Zwaan 2001), it could be confirmed that galaxy groups, with a higher likelihood of galaxy encounters and hence a higher frequency of tidal interactions, harbor extraplanar or extragalactic gas more frequently (Hart et al. 1980; Sancisi et al. 1984; Appleton et al. 1981; Haynes 1981), in particular in compact groups (Allen & Sullivan 1980; Verdes-Montenegro et al. 2001;

Borthakur et al. 2010; Hess et al. 2017). Despite many galaxies being disturbed in their outer HI disks (Huchtmeier & Richter 1982; Briggs 1982), which extend well beyond their optical counterparts, no evidence was found that HI disks of galaxies often connect to a low column density (extragalactic) regime other than tidal debris (Briggs et al. 1980; Haynes 1981; Haynes et al. 1984). Blind Lo & Sargent (1979), Krumm & Brosch (1984), Henning (1992), Henning (1995), Schneider et al. (1998), Hoffman et al. (1992), McMahon et al. (1992), Li & Seaquist (1994), Sorar (1994), Briggs et al. (1997), Rosenberg & Schneider (2000), Koribalski et al. (2003), Kilborn et al. (2005), and pointed (Fisher & Tully 1981a, 1981b) HI surveys were analyzed for the abundance of isolated clouds in various environments, bearing a close to vanishing abundance of dark clouds at higher masses ( $M_{\text{HI}} > 10^9 M_{\odot}$ ). Zwaan et al. (1997) were not able to detect massive, dark, isolated HI clouds in the Arecibo HI strip survey, and even the HI Parkes All Sky Survey (HIPASS; Barnes et al. 2001) was not able to clearly detect any optically dark HI clouds (Banks et al. 1999; Doyle et al. 2005; Karachentsev et al. 2008; Wong et al. 2009) not identifiable as tidal debris (Kilborn et al. 2000; Ryder et al. 2001).

At the low-mass end, Taylor et al. (1995) searched for the existence of intergalactic clouds in the environment of blue compact dwarf galaxies, potentially triggering their starburst activity, without success (Taylor et al. 1996). Other studies found that there is even not much room for a gas-rich low surface brightness dwarf galaxy population (Briggs 1990; Weinberg et al. 1991). While some surveys targeting the galaxy cluster environment seemed initially to be unsuccessful in detecting dark clouds (Dickey 1997; Barnes et al. 1997; van Driel et al. 2003; Pisano et al. 2004), the occasional lower mass clouds could be found (Putman et al. 1998a). It has since become well established that the cluster environment, in which several mechanisms act to remove gas from galaxies and the paths connecting interaction partners are larger, is the preferred environment to find isolated HI clouds (Hoffman et al. 1999; Bravo-Alfaro et al. 2000, 2001). Under which circumstances those clouds can exist as long-lived individual entities or whether they are tidal features (or both in the case of tidal dwarf galaxies) is an ongoing matter of debate. The quest to determine the abundance of dark intergalactic clouds nevertheless continues to trigger new studies, as their existence is cosmologically relevant.

First, the existence of dark matter substructure with masses below those of observed dwarf galaxies is a postulate of the standard galaxy formation theory (Kauffmann et al. 1993; Klypin et al. 1999; Moore et al. 1999). It appears therefore conceivable that dark galaxies exist, which, below a certain mass threshold cease to form stars completely. Dark HI clouds could, in principle, contain gas that is gravitationally bound to a dark matter halo, without the ability to form stars (Verde et al. 2002; Taylor & Webster 2005). Hence, the absence of low-mass galaxies or dark galaxies supports the conclusion that regulatory mechanisms, i.e., a photoionizing background and supernova feedback deplete gas in the lowest-mass halos before a substantial amount of stars can be formed (Larson 1974; Rees 1986; Quinn et al. 1996; Barkana & Loeb 1999; Efstathiou 2000; Gnedin & Kravtsov 2006).

With these regulatory mechanisms becoming a necessity to explain various luminosity and mass functions, the existence of dark galaxies would in turn be a problem for the standard

theory. In fact, claims of the existence of massive dark galaxies or the detection of dark galaxy candidates (Davies et al. 2004; Minchin et al. 2005, 2007; Walter et al. 2005; Oosterloo et al. 2013) triggered a substantial scientific discussion, mainly focusing on the question whether the velocity structure of tidal debris can, in projection, mimic a cold gas disk in stable rotation about a dark matter halo (Bekki et al. 2005b, 2005a; Vollmer et al. 2005; Duc & Bournaud 2008; Taylor et al. 2013, 2017, 2018), rendering the interpretation of a dark cloud as a dark galaxy unlikely.

Second, the abundance and mass distribution of neutral extragalactic gas in various environments and its stability against the various mechanisms of gas depletion can be used to gauge galaxy formation scenarios. While with increasing sensitivity the number of serendipitous detections of dark clouds or condensations in tidal debris increased (Hibbard et al. 2001b, 2001a; Koribalski & Dickey 2004; McKay et al. 2004; Koribalski 2004; Koribalski & Manthey 2005; Kilborn et al. 2006; English et al. 2010), only recently have a substantial number of dark clouds been found in blind HI surveys (see, e.g., Wong et al. 2021).

Most notably, using the 40% release data of the blind Arecibo Legacy Fast ALFA (ALFALFA) survey (Giovanelli et al. 2005), (e.g., Cannon et al. 2015) estimated that less than 1.5% were not associated with stars, and 25% of those could not immediately be identified as tidal features. This triggered a number of follow-up studies of the most intriguing cases (Cannon et al. 2015; Janowiecki et al. 2015; Ball et al. 2018; Leisman et al. 2021), among others unveiling the characteristics of the extreme high-HI mass low-surface brightness (LSB) object AGC 229101, with  $M_{\text{HI}}/M_{*} \approx 70$  and  $M_{\text{HI}} = 10^{9.3} M_{\odot}$ . None of the sources has been found to lack any stellar counterpart, while Kent et al. (2007) and Kent (2010) confirmed the detection of two formerly unknown dark clouds with  $M_{\text{HI}} \leq 10^{8.5} M_{\odot}$  in the vicinity of the Virgo cluster. The second survey turning out a substantial number of dark cloud candidates is the Arecibo Galaxy Evolution Survey (AGES; Auld et al. 2006). Taylor et al. (2012) found seven ( $M_{\text{HI}} \leq 10^7 M_{\odot}$ ) dark clouds in the surroundings of the Virgo Cluster. Taylor et al. (2016) provide a comprehensive list of known dark clouds including AGES detections. Remarkably, dedicated surveys of two rich groups, CVn (Kovač et al. 2009) and UMa (Lang et al. 2003; Wolfinger et al. 2013), detected two small isolated clouds with  $M_{\text{HI}} \leq 10^{7.4} M_{\odot}$ .

In summary, massive ( $M_{\text{HI}} > 10^9 M_{\odot}$ ) optically dark neutral hydrogen clouds (or, rather, candidates for dark clouds) are so rare that they are the subject of individual studies. Most notable, beneath AGC 229101 (Leisman et al. 2021), are the Leo Ring (Schneider et al. 1983; Schneider 1985; Schneider et al. 1986; Schneider 1989) and the double source HI 1225 +01 (Giovanelli & Haynes 1989).

In this paper, we report the discovery of a massive HI cloud that does not appear to have any star formation history, located in a filamentary large-scale structure, and in close proximity to a galaxy group. In the following we describe the radio observations, source extraction, and comparison with deep multiwavelength imaging to discern the nature of the object. Throughout this study, if not stated otherwise, systemic velocities are quoted in the optical convention  $v = cz$ , while line widths are given in the local reference frames. We assume a standard  $\Lambda$ CDM cosmology with  $\Omega_{\Lambda} = 0.73$ ,  $\Omega_{\text{M}} = 0.27$ , and  $H_0 = 70 \text{ km s}^{-1}$ .

## 2. Observations and Data Reduction

The MeerKAT Habitat of Galaxies Survey (MeerHOGS) is an initiative to exploit the sensitivity and  $1^\circ$  field of view of the MeerKAT Square Kilometre Array (SKA) precursor to map local large-scale structures. This study is based on the survey pilot, which targeted a  $\sim 10 \text{ deg}^2$  cosmic filament at redshift  $0.025 < z < 0.034$ , visible in the redshift distributions of the 2dF Galaxy Redshift Survey (2dFGRS; Colless et al. 2001) and Galaxy and Mass Survey (GAMA) G23 surveys (Driver et al. 2011; Liske et al. 2015). For details on the survey layout and the data reduction we refer to Appendix A. Here, we provide a summary.

The observations were centered on the highest concentration of galaxies in the filament, which included a compact group identified using the 2MRS (Díaz-Giménez et al. 2012) at  $z \approx 0.029$ . Within the GAMA survey, this four-member compact group lies at the core of an  $N = 18$  group with a friends-of-friends redshift,  $z_{\text{fof}} = 0.02891$ , identified in the GAMA Galaxy Group Catalog ( $G^3C$ ), which employs an iterative friends-of-friends algorithm (Robotham et al. 2011). Henceforth, we will refer to this group as “Group-83” to match the identification in the  $G^3C$ .

The filament was observed in 20 pointings arranged in a linear fashion along the filament, with five additional pointings in the vicinity of Group-83, in the  $L$ -band with the MeerKAT telescope in 2019 May. The usage of the available 4K correlator mode resulted in a frequency resolution of 209 kHz or  $45.4 \text{ km s}^{-1}$  in the rest frame of an object at  $z \sim 0.029$ . The integration time for each pointing was  $\sim 30$  minutes. While the  $L$ -band frequency range of MeerKAT is 900–1670 MHz, we used only the frequency range 1319.8–1517.1 MHz for the data reduction with the CARACAL (Józsa et al. 2020) radio-interferometric data reduction pipeline. CARACAL performs automated standard calibration and imaging, including flagging, cross-calibration, self-calibration, deconvolution, and mosaicing. For the latter, we additionally employed the EQUOLVER package (see Appendix A) at the time of the data reduction, not yet implemented in CARACAL) convolving the images to a common resolution before mosaicing. The source-finding software SOFIA (Serra et al. 2015) was combined with a Savitzky–Golay (Savitzky & Golay 1964) filter to perform an additional continuum subtraction in the image domain, as well as to identify HI sources in the data cube. Table 1 summarizes the observational parameters. For the channel maps used in this study we obtained an rms of  $0.19 \text{ mJy beam}^{-1}$  at a spatial resolution of  $34''.4 \times 34''.4$ .

## 3. Results

### 3.1. Galaxies in the Vicinity of the Dark Cloud Chain

Initial HI source finding was carried out with SoFiA (see Section A.5). We identified 62 HI sources (of 196 total detections in our HI cube) whose systemic velocities are in the redshift range of the filament:  $0.025 < z < 0.034$  ( $7500\text{--}10,201 \text{ km s}^{-1}$ ). We compared the resultant source positions and velocities with the GAMA G23 redshift catalog using a  $10''$  ( $\sim 6 \text{ kpc}$  at  $z = 0.0295$ ) search radius and  $\pm 180 \text{ km s}^{-1}$  cylinder, finding 46 associations with known galaxies. These associations include galaxies from the 2dFGRS (Colless et al. 2001) that were not included as part of the GAMA science sample. Only galaxies with redshift quality flags  $NQ \geq 3$ , i.e., science quality, are considered.

**Table 1**  
Details of the MeerKAT Observations Used in This Study

Observational Parameters	
Parameter	
Target	MeerHOGS
Observing dates	2019 May 17, 24, 26, 31
Number of pointings	25
Bandpass/flux calibrator	PKS 1934-63
Gain calibrator	J2302-3718
Time spent on each pointing	30.4 minutes
Total observation time	4.5, 4, 4, 4 hr
Available frequency range	900–1670 MHz
Frequency range used	1319.8–1517.1 MHz
Central frequency	1416.8 MHz
Spectral resolution	208.984 kHz
Available number of channels	4096
Number of channels used	959
Number of antennas	58, 58, 64, 58
rms continuum, per pointing	$18 \mu\text{Jy beam}^{-1}$
rms line mosaic	$0.19 \text{ mJy beam}^{-1}$
Mosaic spatial resolution (HPBW)	
continuum	$13''.5 \times 13''.5$
line	$34''.4 \times 34''.4$

**Note.** See Figure 8 for the combined footprint of the 25 pointings. Notice that for a mosaic the rms is variable. In this table we indicate a typical rms as relevant for this study.

During the course of identifying associations, however, we noted a number of HI sources without optical counterparts. Constructing a moment-0 map from the HI cube in the velocity range of the filament, we then compared it to deep optical imaging from the Kilo-Degree Survey (KiDS; Kuijken et al. 2019), sensitive  $3.4 \mu\text{m}$  mid-IR imaging from the Wide-field Infrared Survey Explorer (WISE; Wright et al. 2010) and far-UV (FUV)/near-UV (NUV) imaging from the Galaxy Evolution Explorer (GALEX; Martin et al. 2005). We discovered a relatively massive HI source (or complex of sources) that did not have a definitive counterpart in the UV, optical, or infrared imaging, nor in the radio continuum image produced from these MeerKAT observations (Yao et al. ApJ submitted). We dub this complex the *dark cloud chain* or *dark cloud complex* throughout this paper.

In the rest of this section we lay out the nature of this dark cloud complex as follows. We first consider the larger environment to put the cloud complex into context, particularly with respect to the neighboring galaxy groups. We then demonstrate the robustness of the HI cloud complex, including after-the-fact confirmation with HIPASS data. Finally, we limit the possibility of stellar counterparts using NUV, optical, and IR imaging.

MeerHOGS was designed to target a foreground large-scale filament at  $z \sim 0.03$ , in which the dark cloud chain is centrally located. We consider the environment of the dark chain to ascertain its possible origin scenarios, focusing only on the redshift range  $0.025 < z < 0.034$ . Within the GAMA G23 region we benefit from high redshift completeness, 98% for 19.2 mag in the  $r$  band (Liske et al. 2015), and therefore superior environment measures; for instance, the  $G^3C$ , which employs an iterative friends-of-friends algorithm (Robotham et al. 2011).

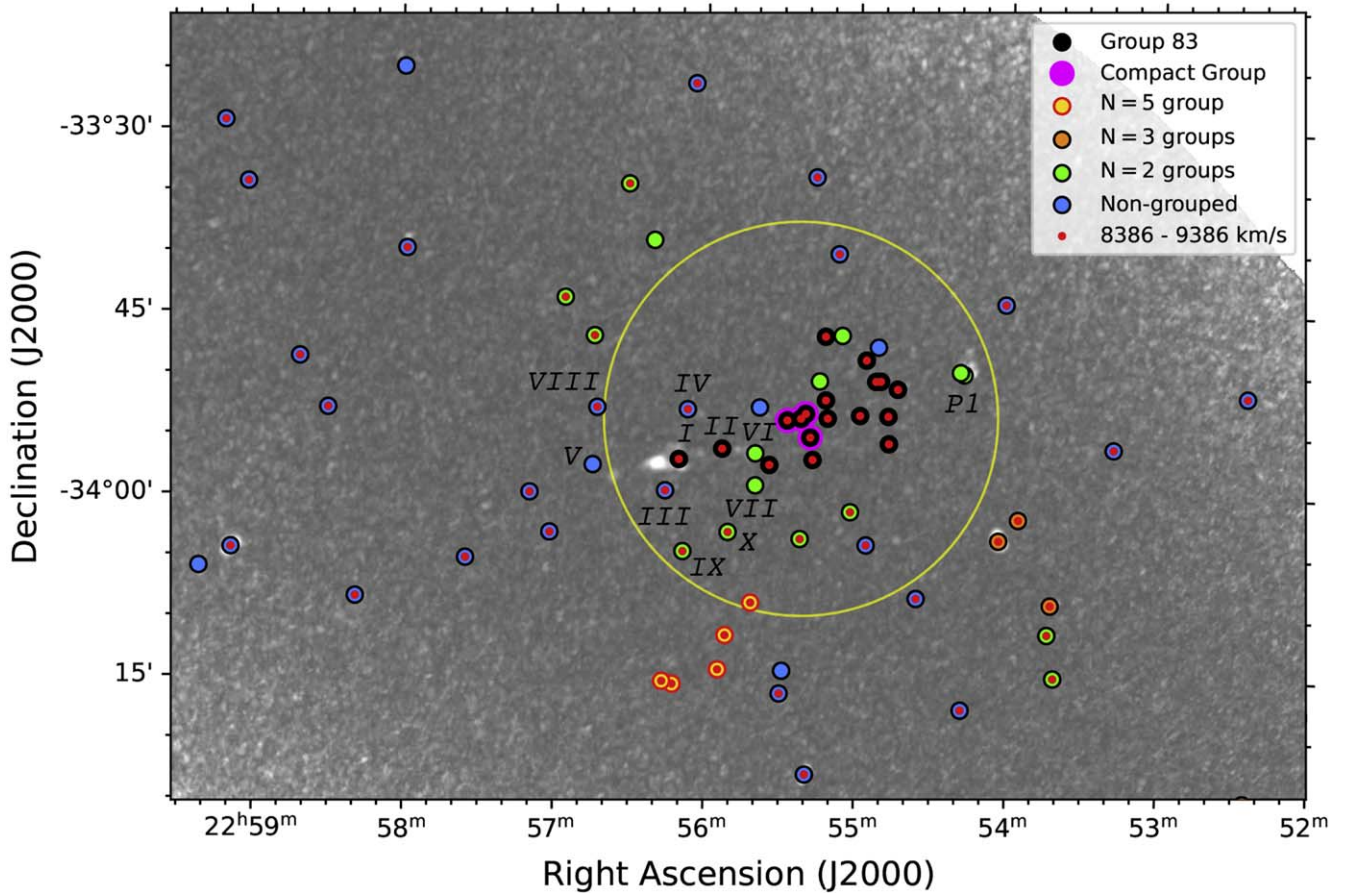


**Figure 1.** The immediate environment of the dark chain within the  $0.025 < z < 0.034$  redshift range, highlighting different groupings of objects in the filamentary structure. The grayscale image is the HI moment-0 map whose column density ranges between  $1$  and  $25 \times 10^{19}$  atoms  $\text{cm}^{-2}$ , the dark cloud chain is the most massive gas complex in the region. The black points denote GAMA Group-83, an  $N = 18$  group with  $z_{\text{tof}} = 0.02891$  ( $8667 \text{ km s}^{-1}$ ), where the yellow circle (centered on the group) is  $0^{\circ}26$ ,  $\sim 0.56$  Mpc radius, which corresponds to the  $R_{200}$  of Group-83. Galaxies with velocities within  $\pm 500 \text{ km s}^{-1}$  of the dark chain ( $8886 \text{ km s}^{-1}$ ). Labels I–X indicate the position of galaxies in the projected proximity of the dark HI chain ( $9' \sim 320 \text{ kpc}$ ) as discussed in Section 3. See Table 2 for additional information.

Figure 1 shows a HI moment-0 map of the central region of the MeerHOGS field where our HI observations are the most sensitive. The dark cloud chain is located within or very close to GAMA Group-83 (black points), a  $N = 18$  galaxy group with a *friends-of-friends* redshift of  $0.02891$  ( $8667 \text{ km s}^{-1}$ ). The originally targeted compact group is at its core (magenta points in Figure 1), with the brightest cluster galaxy of the group as one of the members of the compact group (which includes the galaxy, IC 5262). Other galaxies within the  $G^3C$  in this redshift range are demarcated according to their group size, (green, orange, and yellow) with non-group galaxies shown as blue points. Labels I–X indicate the position of galaxies in the projected proximity of the dark HI chain ( $9' \sim 320 \text{ kpc}$ ); we provide additional information for these select galaxies in Table 2, including the GAMA identification and coordinate position, optical redshift, and velocity. Velocity errors from the GAMA-AAOmega spectra are individually calibrated for each spectrum using AUTOZ (Baldry et al. 2014), whereas redshifts observed as part of 2dFGRS subsumed into the GAMA survey (Baldry et al. 2010) are assigned an error of  $85 \text{ km s}^{-1}$  (see Colless et al. 2001).

The gas complex ranges in column density up to  $25 \times 10^{19}$  atoms  $\text{cm}^{-2}$  and has a systemic velocity of  $\sim 8886 \text{ km s}^{-1}$  ( $z = 0.0296$ ); galaxies within  $500 \text{ km s}^{-1}$  of the complex are marked with a red dot in Figure 1. The dark chain lies at the eastern edge of the large group, Group-83,

notably close to member I ( $z = 0.02805$ ) and member II ( $z = 0.02860$ ); see Table 2. Further to the group members are the non-grouped galaxies III, IV, and V with redshifts of  $0.02920$ ,  $0.02806$ , and  $0.03274$ , respectively. We note that no member of Group-83, nor galaxy III or IV have an HI detection. Galaxy V is therefore the exception, but with a redshift well distant of the dark cloud. The only other notable detection of HI in this region is the interacting pair of galaxies (P1 in Figure 1; Pair 1 in Table 2) on the opposite side of Group-83 to the dark chain. However, these galaxies lie in front of the dark chain, offset by  $\sim 600 \text{ km s}^{-1}$ .

We note that the  $R_{100}$  (i.e., the group radius defined by the most distant member from the iterative center determined for the group) for Group-83 is  $0.36 \text{ Mpc}$ , and has a derived velocity dispersion of  $228.6 \text{ km s}^{-1}$  (similar to the cloud velocity width) and dynamical mass of  $10^{13.5} M_{\odot}$ . Further, assuming an isothermal distribution, the  $R_{200}$ , which follows from the relation  $\frac{\sqrt{3} \sigma_{\text{gr}}}{10 H(z)}$ , has a value of  $0.56 \text{ Mpc}$  (shown as the yellow circle in Figure 1). Furthermore, we note the velocity difference between the central gas concentration and the Group-83 center is  $\sim 200 \text{ km s}^{-1}$ , which is smaller than the group dispersion. Consequently, the dark cloud chain is well within the gravitational influence of the group, and likely the compact core at the center.

**Table 2**  
Galaxies within Projected Proximity of the Dark HI Chain ( $9' \sim 310$  kpc at the Distance of the Central Concentration of the HI Cloud Chain)

Investigating Possible Associations of the Dark Chain					
Identifier	CATAID	R.A.	Decl.	$z_{\text{helio}}$	$cz$
		deg	deg	...	$\text{km s}^{-1}$
Group-83 galaxies					
Galaxy I	5256498	344.04430	-33.95156	0.02805	$8409 \pm 85$
Galaxy II	5256643	343.97295	-33.93668	0.02860	$8574 \pm 25$
Ungrouped galaxies					
Galaxy III	5256376	344.06646	-33.99435	0.02920	$8754 \pm 85$
Galaxy IV	... <sup>a</sup>	344.03040	-33.88321	0.02806	$8412 \pm 85$
Galaxy V	5256491	344.18659	-33.95962	0.03274	$9815 \pm 25$
Galaxy VIII	5256924	344.17966	-33.88105	0.02820	$8454 \pm 85$
Pairs					
Galaxy VI	5256517	343.91816	-33.94274	0.02723	$8163 \pm 85$
Galaxy VII	5256426	343.91790	-33.98653	0.02730	$8184 \pm 35$
Galaxy IX	5255926	344.03695	-34.07758	0.02814	$8436 \pm 85$
Galaxy X	5256135	343.96247	-34.05080	0.02868	$8598 \pm 25$
Pair 1	5241095	343.58043	-33.82934	0.02742	$8221 \pm 25$
	5240983	343.57447	-33.83238	0.02733	$8194 \pm 24$

**Note.** The CATAID corresponds to the GAMA identification and  $V_{\text{optical}}$  corresponds to the heliocentric velocity.

<sup>a</sup> This galaxy does not have a CATAID as it was not included in the GAMA main survey sample selection (Baldry et al. 2010); the redshift is from 2dFGRS (Colless et al. 2001).

### 3.2. HI Properties of the Dark Cloud Chain

First shown at the center of the HI map (Figure 1), the HI dark cloud complex extends approximately  $10'$  from east to west and across only a few ( $\sim 3$ – $4$ ) channels in velocity, or roughly  $<136$ – $182 \text{ km s}^{-1}$  in width, for any given region of the cloud complex. This is also shown in Figure 2, a cutout of our data cube in the region and velocity range of the cloud complex. The channel maps reveal very little kinematic variation across the cloud from east to west.

We will now focus on characterizing the gas cloud complex using an integrated map that delineates the diffuse from clumpy components.

For a range in velocity that takes into account this lateral east–west geometry of the cloud relative to the plane of the sky,  $8682$ – $9057 \text{ km s}^{-1}$ , we construct a detailed view of the cloud complex using a moment-0 mapping technique in which we integrate 3 channels along the line of sight where the emission is peaking. In this way we maximize the emission signal-to-noise ratio (S/N) for each spatial pixel of the HI map without the use of a mask. Under the usual assumption that the observed HI is optically thin, the moment-0 map is then converted into a column density map in units of atoms per square centimeter.

The resulting detailed multiwavelength view of the immediate complex is shown in Figure 3, featuring in the first panel the HI moment-0 map overlaid with red contours of gas column density ( $3, 5, 8, 14,$  and  $23 \times 10^{19} \text{ atoms cm}^{-2}$ ). The rms noise is about  $0.9 \times 10^{19} \text{ atoms cm}^{-2}$ , and hence the lowest contour is approximately at the  $3\sigma$  level. We identify at least seven local maxima, labeled (a)–(g) in Figures 2 and 3. The single constituents of the complex have a similar shallow kinematic depth of  $3$ – $4$  channels, or  $<182 \text{ km s}^{-1}$ , partly showing spurious kinematic signatures indicating systematic motion in

parts of the whole complex, most notably between Sources (f) and (g), although a general tendency is hard to discern. More clearly, the whole complex, appearing in 5 channels ( $\sim 227 \text{ km s}^{-1}$ ) shows an east–west velocity gradient (refer also to Figure 2); note that the complex appears in 5 channels, while the depth for any given location in the cloud is  $3$ – $4$  channels in width), again rendering the detection a real feature, as this would be hard to mimic by measurement errors or data reduction artifacts.

Supplemental to the channel maps and the multiwavelength maps, we present a RA-velocity diagram that again reveals the dark cloud chain emission maxima in addition to its kinematical structure. The diagram, shown in Figure 4, has panels (slices) of decl., chosen to highlight each individual maxima, from (a)–(g); see also the moment-0 map in Figure 3 and the 3D version shown below in Figure 9. The diagram clearly shows the resolved, filamentary or chain-like morphology of the gas, extending from east to west. It is also clear that there is a lack of kinematic structure (it is relatively flat in velocity,  $\sim 110 \text{ km s}^{-1}$  ( $108 \text{ km s}^{-1}$  from source (a) to source (g), see also Table 3) and shows little gradient from one decl. slice to the next (best seen in Figure 9).

Focusing on the first panel showing the HI distribution (Figure 3(a)) the brightest and largest source is Source (b), which is resolved, while the other sources may be unresolved, but also embedded within diffuse emission. SoFiA was unable to automatically deblend this complex morphology. Consequently, we used a new visualization tool to identify and divide the local maxima into seven discrete sources. Developed specifically for spectral-imaging data interaction, and notably with HI cubes, the virtual reality (VR)-based software suite called *iDaVIE*<sup>18</sup> (Jarrett et al. 2021) was deployed to separate

<sup>18</sup> <https://idavie.readthedocs.io/en/latest/>

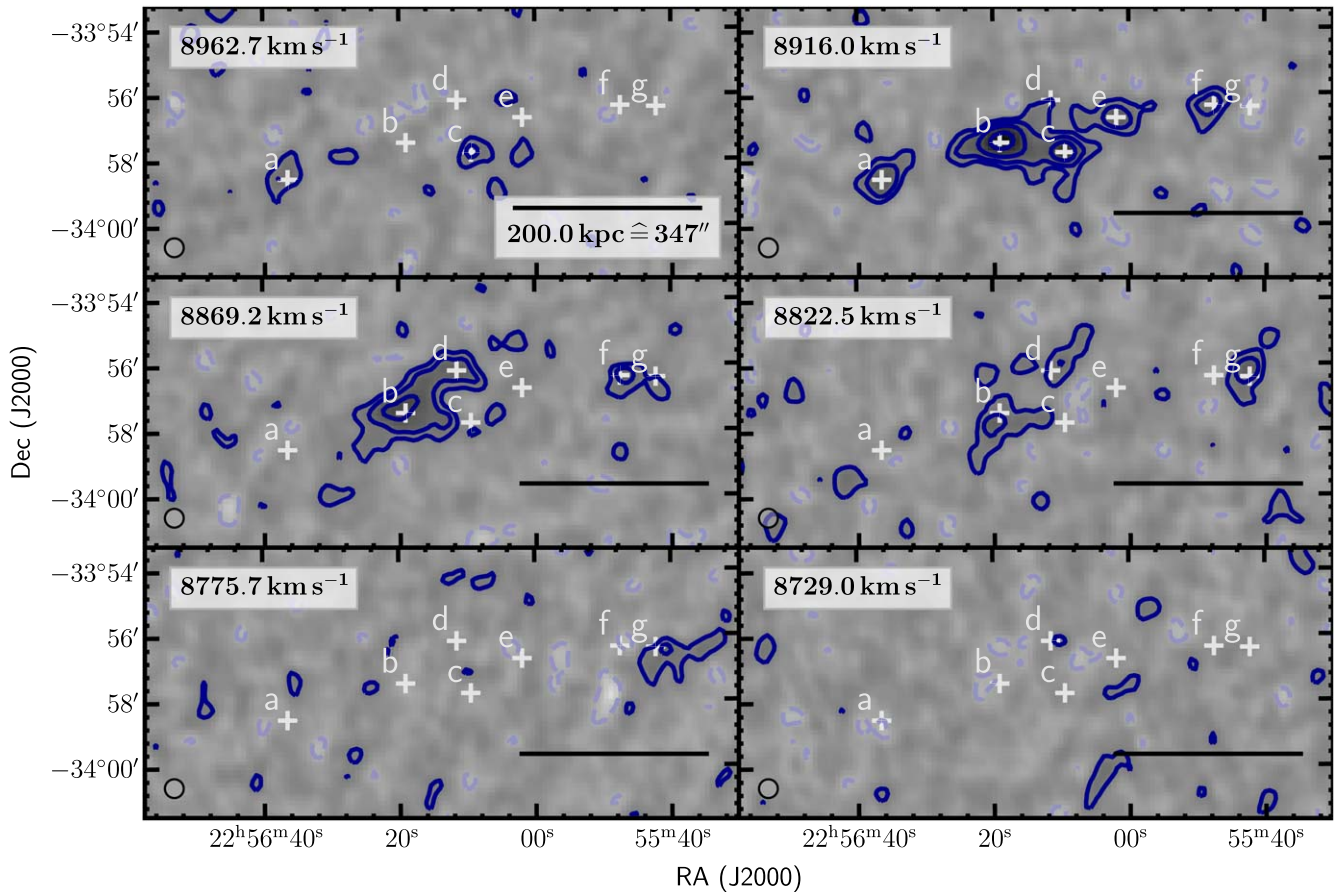


**Figure 2.** Observed HI data cube in the region and velocity range of the dark cloud chain. Contours denote the  $-0.38, 0.38, 0.76, 1.52,$  and  $3.04 \text{ mJy beam}^{-1}$  levels ( $-2, 2, 4, 8, 16 \sigma_{\text{rms}}$ ), negative contours are dashed. White crosses mark HI detections (labeled (a)–(g); see Table 3). The black circle in the lower left of each panel indicates the spatial resolution (HPBW). The scale bar indicates 200 kpc. The massive central concentration (Source b) has a peak intensity in the second velocity channel ( $8916 \text{ km s}^{-1}$ ).

the seven sources using mask-editing functionality in which the VR user is able to create (or modify) a mask that specifies which HI intensity voxels (3D pixels) belong to which sources. More details of this mask-editing procedure and the resulting mask that was used to extract the source characterization is presented in Appendix B.

Source extraction was then carried out using this mask created for the cloud complex. Basic source properties are given in Table 3, including coordinates, spatial sizes, kinematics, column density, and finally, integrated flux and corresponding HI mass (see caption for details). Here, the mass is derived from the integrated flux using the standard equation (assumes optically thin emission):  $\frac{M_{\text{HI}}}{M_{\odot}} = 2.356 \times 10^5 \frac{F_{\text{tot}}}{\text{Jy km s}^{-1}} \frac{D_L}{\text{Mpc}}$ , where the total flux,  $F_{\text{tot}}$ , is integrated over all pixels and all channels (measuring the channel width in radio convention) and scaling for the beam factor, and the luminosity distance,  $D_L$ , in megaparsecs, using the optical redshift corrected to the cosmic microwave background frame. The total mass of the dark cloud chain is  $10^{10.0} M_{\odot}$ , with the masses of the concentrations ranging between  $10^{8.75}$  and  $10^{9.7} M_{\odot}$ .

The noise level (per voxel) of the HI distribution in close vicinity to the dark cloud chain is  $\sim 0.9 \times 10^{19} \text{ atoms cm}^{-2}$ , and correspondingly the uncertainties for the integrated fluxes are well below 10%. However, since these sources are not well defined, but include both discrete and nebulous emission with connections between them, these source measurements are only

approximate—clearly there is overlap and blending systematics between sources that dominate the accuracy of the fluxes and the derived HI mass.

**HIPASS:** Such a massive HI cloud may be marginally detected in the single-dish HIPASS survey. We subsequently searched the HIPASS and HICAT catalogs (see, for example, Barnes et al. 2001) for any counterparts. There were none, and notably with few cataloged sources at such large systemic velocities. Searching through the HIPASS Public Data Release<sup>19</sup> spectra, we identified a possible detection in HIPASS cube “H187” at the position of the dark cloud chain. Prompted by this encouraging result, we obtained an improved cube used to make HICAT (Meyer et al. 2004). We then extracted a spectrum centered on the spatial and velocity coordinates of Source (b). We show the resulting spectrum in the velocity range of the cloud in Figure 5. Details and a wideband spectrum are given in Appendix C. Here, we summarize the results: fitting and removing the underlying ripple continuum, we measure a peak flux, at  $\sim 8886 \text{ km s}^{-1}$ , to be  $0.038 \text{ Jy beam}^{-1}$  with a S/N of  $\sim 4.2$ . Integrating the spectrum channels, across  $\pm 150 \text{ km s}^{-1}$  centered on the cloud systemic velocity, the integrated flux is  $2.9 \pm 0.6 \text{ Jy km s}^{-1}$  at the  $5\sigma$  level, a likely detection of the HI gas cloud. For the MeerKAT observations, we measure the integrated flux of Source (b) to be  $1.4 \text{ Jy km s}^{-1}$ , and of the entire complex to be  $\sim 2.8 \text{ Jy km s}^{-1}$ .

<sup>19</sup> <https://www.atnf.csiro.au/research/multibeam/release/>

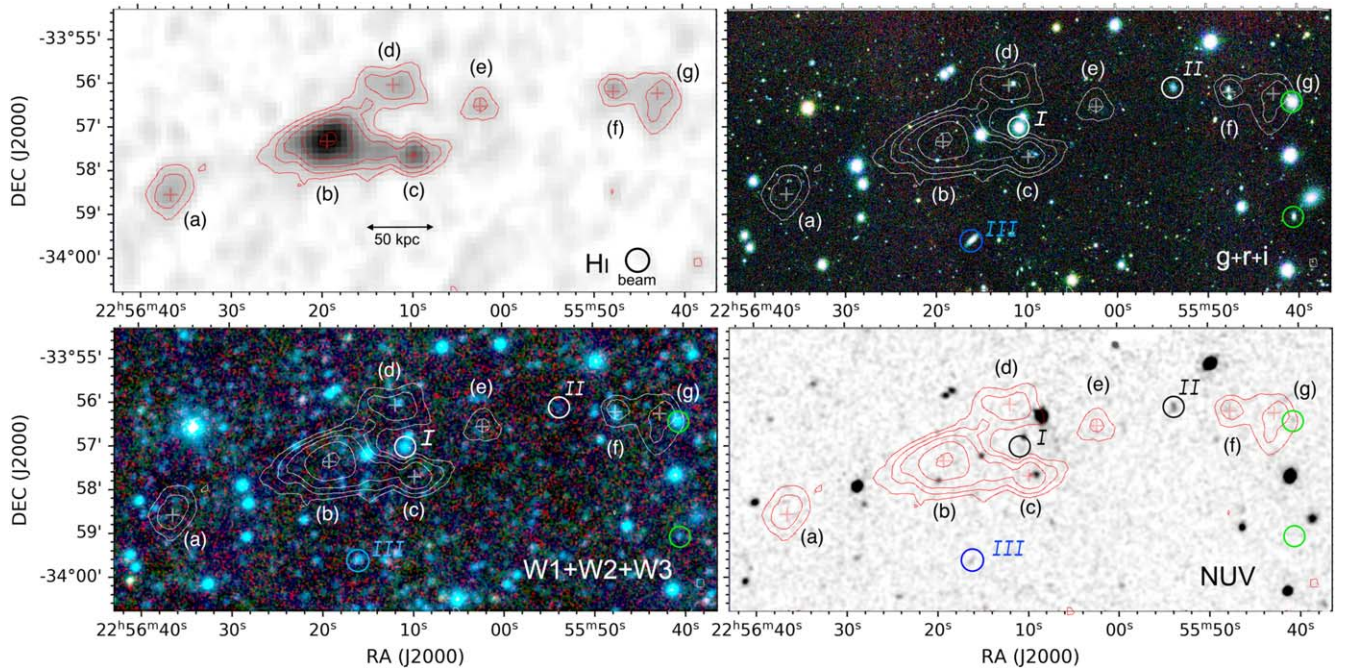


**Figure 3.** Dark cloud chain as seen across the electromagnetic spectrum. The four panels show the H I column density map (upper left; 8817–8931 km s<sup>-1</sup> with rms noise  $\sim 0.9 \times 10^{19}$  atoms cm<sup>-2</sup>), KiDS  $g,r,i$  bands (upper right), WISE 3.4–12  $\mu$ m bands (lower left) and GALEX NUV (lower right). Contours of the H I column density are overlaid on all four maps, with values of 3, 5, 8, 14, and  $23 \times 10^{19}$  atoms cm<sup>-2</sup>. Red/white crosses demark H I detections (labeled (a)–(g); see Table 3), and the small circles denote filament galaxies as marked in Figure 1 (blue is non-group; black/white is group; green are galaxy pairs). The closest Group-83 galaxy to the H I is labeled I ( $z = 0.02805/8415$  km s<sup>-1</sup>), just west of the massive gas complex. Other nearby group galaxies are labels II ( $z = 0.0286/8580$  km s<sup>-1</sup>) and III ( $z = 0.0292/8760$  km s<sup>-1</sup>). The central H I source (Source (b)) is not detected in any band.

The single-dish results are therefore consistent with the aggregate interferometric measurements, given the large Parkes telescope beam ( $\sim 15.5'$ ) and its sensitivity to low column density gas in the vicinity of the dark cloud chain. Moreover, the good agreement leaves very little room for an additional low column density component undetected by MeerKAT.

Next, we carried out a multiwavelength analysis to interrogate the nature of the cloud complex. In Figure 3 (panels (b)–(d), respectively) we compare the neutral gas distribution with deep  $g,r,i$ -band imaging from KiDS-S ( $g,r,i$  bands; de Jong et al. 2017; Kuijken et al. 2019), WISE mid-infrared (W1, W2, and W3, covering 3.4–12  $\mu$ m; Wright et al. 2010), and the ultraviolet GALEX (NUV; Martin et al. 2005), where the red H I contours of column density are repeated in all four panels for juxtaposition purposes.

Comparing the H I emission to the UV, optical, or IR imaging reveals that counterparts are not detected (with one possible exception, see below). Most notably, the large central Source (b) has no counterpart whatsoever. This is surprising given the measured gas mass,  $10^{9.7} M_{\odot}$ , which is typical for a large, gas-rich galaxy, and the depth of the imaging (details below), which suggests a very high gas mass-to-light ratio, and very little, if any, star formation history. The closest known galaxy is labeled I in the diagram, a gas-poor passive galaxy located  $>70$  kpc from the cloud core (see Table 2). The other bright sources in the field are foreground stars, most easily seen in the WISE 3-color image, Figure 3(c) (stars very clearly appear as bright *blue* point sources). Finally, we highlight Source (c), just to the west of the massive central cloud—it is the second brightest source in the seven, and it may be associated with a faint optical galaxy (discussed below).

The gas complex is located at the edge of the Group-83. We find it intriguing that the dark cloud chain has a long

filamentary appearance, stretching from east to west, and pointing exactly toward the location of the core of Group-83 (see Figure 1). Given the relatively *flat* kinematics (Figure 2)—limited motion along the radial line of sight—and the long chain extending over  $\sim 400$  kpc (396 kpc from Source (a)–(g)) toward the group center (Figures 1 and 3), it suggests a tantalizing dynamic link to the galaxy overdensity, taking into account the slight gradient along the filament, either lateral accretion toward it or expulsion away from it. However, neither the nature of the dark cloud, nor its physical connection to the group is certain. Next, we consider the multiwavelength information in quantitative detail.

### 3.3. Massive Dark Cloud: Gas versus Star Formation History

The chain of H I ranges in peak column density from  $7\text{--}25 \times 10^{19}$  atoms cm<sup>-2</sup>, and in integrated masses from  $10^{8.7}\text{--}10^{9.7} M_{\odot}$ ; see Table 3. For normal ranges of gas mass relative to optical luminosity ( $M/L$ ), and column densities that indicate relatively clumpy gas, these objects should be easily detected in the optical, assuming they have formed stars as galaxies. The optical  $g,r,i$  bands are sensitive to moderate-age (5 Gyr) starlight and to young (10 Myr) star formation (through the blue continuum and H $\alpha$ +[N II] emission). At 3.4  $\mu$ m, the infrared map is sensitive to the old (11–13 Gyr) stellar population, while the NUV map is sensitive to recent (100 Myr) star formation; hence, the set of maps cover most of the star formation history of a galaxy. Figure 3 reveals very little correspondence between the gas and extragalactic emission at any wavelength.

If we consider first the footprint of the dark cloud, denoted as (b) in Figure 3(a), it extends over 50 kpc in diameter, likely larger still if we follow the emission down to the noise of the

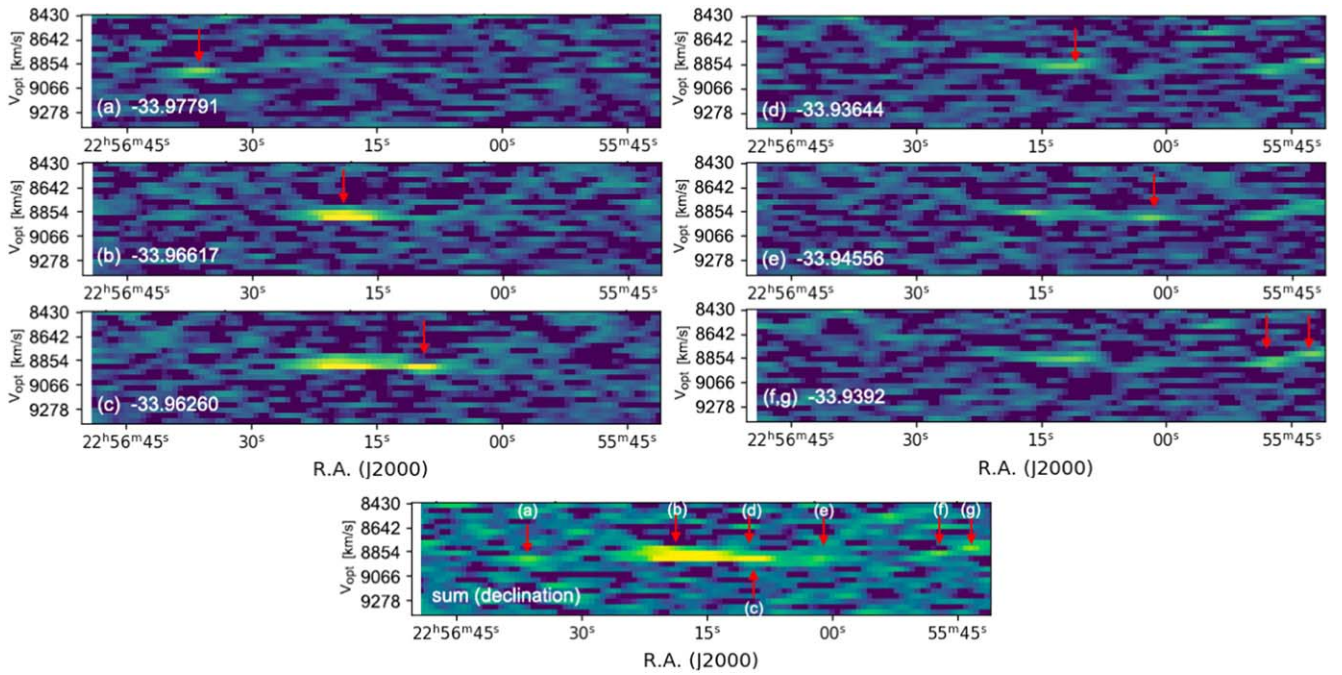


**Figure 4.** Position-velocity diagram for the dark cloud chain. The top six panels have specific declinations (deg J2000) to highlight the HI emission maxima: (a)–(g), which run from east to west. The bottom panel is the sum across the decl. channels  $-33.990^\circ$  to  $-33.936^\circ$ . The red arrows indicate where the maxima are located in the RA-velocity plane. Note the filamentary structure along the east–west direction, and the lack of kinematic variation across the cloud complex.

map ( $\sim 0.9 \times 10^{19}$  atoms  $\text{cm}^{-2}$ ). At the center of this gas cloud, there are no detections in any other band (Figures 3(b)–(d)), even at the faintest flux levels, or using aggressive smoothing to increase the S/N of any faint emission. This is readily apparent if we zoom into the cloud core using the deep KiDS imaging, see Figure 6.

The deepest optical imaging we have available are from the KIDS DR4 Kuijken et al. (2019), with  $r$ -band magnitudes reaching 25.2 mag (AB;  $5\sigma$ ) in a small aperture due to the high-quality sub-arcsec seeing. The “g” and “i” bands have similar limiting magnitude depths. In the zoomed color composite (Figure 6), we see a number of small sources, similar in number density to the field outside of the cloud region. None have matches in the GAMA spectroscopic catalog (see below), so their true nature is not certain. We can say that none are in close proximity to the HI core ( $>20 \times 10^{19}$  atoms  $\text{cm}^{-2}$ ) of Source (b). We are able to recognize disk and ellipsoid galaxies, both their size and red (passive) color indicating likely background galaxies. On the periphery of Source (b), near the outer HI contours, there are faint and compact bluish sources that may be star-forming galaxies that are distant, or dwarf galaxies in proximity to the  $z = 0.03$  filament, or most intriguingly, may be star-forming complexes or knots associated with the HI gas cloud. The most promising blue blob to follow up is at  $22^{\text{h}}56^{\text{m}}20^{\text{s}} -33^{\text{d}}58^{\text{m}}08^{\text{s}}$  (J2000), ideally with spectroscopy, but in more practical terms, deeper optical imaging should be carried out to reveal if there other knots or blobs that would indicated an ultra-diffuse galaxy in proximity to Source (b).

We have made use of a photometric redshift catalog to investigate the sources in the vicinity of the cloud chain. We find no obvious associations with the cloud or filament at  $z = 0.03$ . GAMA provides EAZY (Brammer et al. 2008) photometric redshift estimates for all optical/near-IR detections (Bellstedt et al. 2020), which are based on fits to the  $u$ – $K$  spectral energy distributions (for details see Driver et al. 2021,

under review). For the sources near the central cloud core (Figure 6, within the three inner contours, or  $>5 \times 10^{19}$  atoms  $\text{cm}^{-2}$ ), the GAMA DR4 photo- $z$ ’s range from 0.3–0.6, which very likely rules them out as potential associations even given the 10% uncertainty in the photo- $z$ ’s.

Considering the filament galaxies, the nearest Group-83 galaxy members are indicated in Figure 1, located within  $500 \text{ km s}^{-1}$  of the cloud central velocity; most notably, the bright I, II, and III galaxies (see also Figure 3(b) and Figure 6, and properties in Table 2). Nearest, galaxy I is about  $2'$  from the cloud core, and its velocity is such that it would be located at least 70 kpc distant from the cloud core (barring peculiar motions). Their association with the cloud may only be gravitational; they do not appear to be *hosts* for the cloud at the current epoch that is observed. Except for III, which is a small disk galaxy, they are gas-poor and passive in star formation properties (i.e., they are old, evolved galaxies). However, given their proximity to the cloud chain, past tidal interaction may have occurred, and moreover HI gas may have been disruptive to later form the clouds. We discuss such a scenario below (Section 4), notably comparing with the Leo Ring system.

We tentatively conclude that the dark cloud is not detected at wavelengths that we associate with extragalactic emission from stars and the interstellar medium. The imaging does, however, provide an estimate for an upper limit flux for the detection, from which we may then examine the implied ratio between the gas mass and the stellar luminosity (i.e.,  $M_{\text{HI}}$  mass versus optical or infrared luminosity).

Here, we consider the deep  $r$ -band image (Figure 3, upper right panel, and Figure 6). In the vicinity of the dark cloud, we measure a background  $1\sigma$  noise of  $25.6 \text{ mag arcsec}^{-2}$  ( $0.21 \mu\text{Jy mag arcsec}^{-2}$ ), which translates to a  $3\sigma$  detection of  $24.4 \text{ mag arcsec}^{-2}$  considered over a  $25 \text{ arcsec}^{-2}$  area. At the luminosity distance of the dark cloud, 126 Mpc, the corresponding absolute magnitude is  $-11.1 \text{ mag}$ , corresponding to a

**Table 3**  
H I Measurements and Source Properties of the Dark Cloud Chain

H I Detections in the Cloud Chain													
Source	Designation	R.A. Decl. deg	$V_{\text{radio}}$ $\text{km s}^{-1}$	$V_{\text{opt}}$ $\text{km s}^{-1}$	$w_x$ "	$w_y$ "	$w_z$ $\text{km s}^{-1}$	$w_{20}$ $\text{km s}^{-1}$	$I_{\text{peak}}$ $10^{19} \text{ cm}^{-2}$	$F_{\text{tot}}$ $\text{Jy km s}^{-1}$	$D_L$ Mpc	$\text{Log} M_{\text{H I}}$ $M_{\odot}$	
(a)	J22563653-3358328	344.15222-33.97579	<b>8673</b>	<b>8931</b>	80	80	136	106	8.77	0.200	126.6	8.88	
(b)	J22561910-3357270	344.07962-33.95752	<b>8630</b>	<b>8886</b>	200	128	182	139	26.26	1.353	125.9	9.70	
(c)	J22560952-3357456	344.03967-33.96267	<b>8657</b>	<b>8914</b>	104	88	182	105	16.05	0.374	126.4	9.15	
(d)	J22561155-3356098	344.04813-33.93608	<b>8604</b>	<b>8858</b>	104	80	182	132	10.98	0.357	125.5	9.12	
(e)	J22560193-3356425	344.00806-33.94515	<b>8651</b>	<b>8908</b>	88	72	136	86	7.32	0.181	126.3	8.83	
(f)	J22554753-3356212	343.94806-33.93924	<b>8639</b>	<b>8895</b>	72	56	182	110	8.85	0.151	126.1	8.75	
(g)	J22554226-3356236	343.92612-33.93991	<b>8565</b>	<b>8817</b>	64	64	182	135	8.18	0.189	124.9	8.84	

**Note.** See Figure 3 for Source (a)–(g) identifications. The formal *designation* should have the prefix “MHGS” to signify a MeerHOGS source. The widths represent the mask limits (x, y, z respectively) of the source measured from the H I cube; see more details of the mask in the Appendix B. The noise level (per voxel) of the H I distribution in vicinity of the dark cloud chain is  $\sim 0.9 \times 10^{19}$  atoms  $\text{cm}^{-2}$ , and the uncertainties for the integrated fluxes are  $< 10\%$ , although the blending systematics between sources will dominate the accuracy of the fluxes and the derived H I mass. No attempt has been made to correct  $w_z$  or  $w_{20}$  for instrumental broadening.

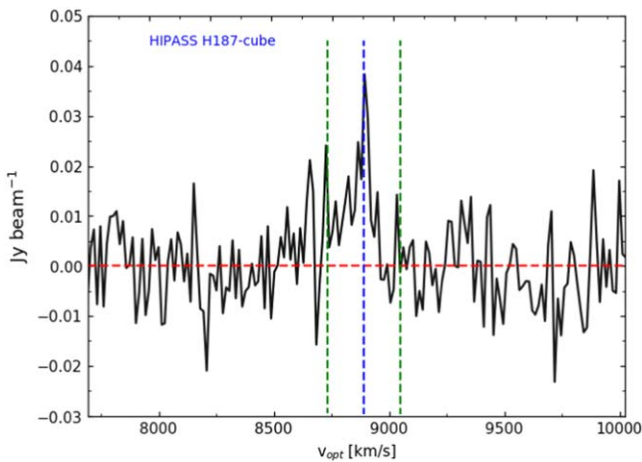


**Figure 5.** H I spectrum of the dark cloud chain as measured using the HIPASS cube H187. The variation in the underlying continuum has been fit and removed. The source is clearly detected at the spatial, R.A., decl. [deg J2000] = 344.080,  $-33.958$ , and velocity coordinates of the massive H I Source (b) (see blue vertical line at  $v_{\text{opt}} = 8886 \text{ km s}^{-1}$ ). The green lines demark the velocity limits for the spectrum integral.

luminosity of  $10^{6.3} L_{\odot}$  (where we have used a zero-point AB magnitude of 4.65). This would be a very low-mass, dwarf galaxy. Now comparing this  $3\sigma$  luminosity limit to the H I mass of the dark cloud (b),  $10^{9.70} M_{\odot}$ , the implied  $M_{\text{H I}}/L_r$  is at least  $\sim 2600$ . Even at a higher detection limit, say  $5\sigma$  surface brightness ( $23.8 \text{ mag arcsec}^{-2}$ ), the implied  $M_{\text{H I}}/L_r$  is greater than 1000.

Consider the mass ratio for Source (b). Using the  $3\sigma$   $r$ -band luminosity and a dwarf galaxy stellar  $M/L = 2$  (Martin et al. 2008; Flynn et al. 2006), the limiting stellar mass is  $10^{6.6} L_{\odot}$ , and the ratio between the neutral gas and the stellar content,  $M_{\text{H I}}/M_{\star}$ , is  $10^{3.1}$ . The extremely high mass ratio is well outside of any scaling relation, and is an order of magnitude larger than the estimated value for the recently discovered massive dark cloud, AGC 229101 (Leisman et al. 2021). We note that the stellar  $M/L$  for dwarf disks and spheroidals may range widely, over an order of magnitude; conservatively using a range between 1 and 10 (e.g., see Flynn et al. 2006), the corresponding range in  $M_{\text{H I}}/M_{\star}$  is  $10^{2.4}$ – $10^{3.4}$ .

Given the absence of a detection, and if we assume the dark cloud is a galaxy with a past history, we can then expect it to be very low mass and low surface brightness, and likely well

resolved by the KiDS imaging. An ultra-diffuse galaxy (UDG) would have an angular size that ranges from a  $\sim$ few to  $13''$  at the distance to the dark chain (see, e.g., the UDG size distribution in van Dokkum et al. 2015 or the sizes of H I-bearing UDGs in Leisman et al. 2017). Even comparing to the classic LSB galaxy, Malin-1, it has a central surface brightness close to  $26 \text{ mag arcsec}^{-2}$  (in the  $V$  band; Bothun et al. 1987), slightly fainter than our KiDS image sensitivity (note, however, the correlated pixels from such a large object would bin up and be easily detected with KiDS).

Nevertheless, binning up the images to effectively smooth the background and peak up any diffuse emission lurking in the noise, reveals nothing at the location of the dark cloud, not even a hint of a faint smudge. Similarly in the  $g$  and  $i$  bands. It is fair to say this large gas cloud is extremely dark in comparison to the optical emission. There may in fact not be any past star formation. A deeper optical image, reaching at least  $27$ – $28 \text{ mag arcsec}^{-2}$  is in order to probe for even lower mass systems.

At the longer wavelengths, the situation does not change. Consider the mid-infrared WISE  $W1$  image; Figure 3(b). It has a  $3\sigma$  surface brightness of  $22.7 \text{ mag arcsec}^{-2}$  (Vega;  $0.26 \mu\text{Jy arcsec}^{-2}$ ), which is also very faint and implies a high mass-to-light ratio. Estimating the ratio using a more conservative  $5\sigma$  limit of  $22.2 \text{ mag arcsec}^{-2}$  (Vega;  $0.4 \mu\text{Jy arcsec}^{-2}$ ), the absolute magnitude for this limit is  $-13.3 \text{ mag}$  (Vega), and the corresponding in-band luminosity (adopting a zero-point magnitude of 3.24, see Jarrett et al. 2013) is  $10^{6.6} L_{\odot}$  (which also implies a low stellar mass,  $\sim 10^{6.3} M_{\odot}$ ). The implied  $M_{\text{H I}}/L_{\text{IR}}$  is  $\sim 1300$ , similarly extreme as what was found in the optical comparison.

#### 3.4. Associations for the H I Chain Sources?

It is clear that the central concentration to the chain of H I detections is not obviously detected in the UV, optical, or infrared, making it a massive, truly dark cloud object (Figure 6). Here, we examine the other sources detected in H I denoted as Sources (a)–(g); see Table 3 and Figure 6.

Source (a) has a peak column density of  $8.8 \times 10^{19}$  atoms  $\text{cm}^{-2}$  and a total atomic hydrogen mass of  $10^{8.88} M_{\odot}$ . It has a lower peak column density compared to the main cloud, and appears much more diffuse in nature. At this central position, and within some arcminutes radius, there are no optical, infrared, or UV detections whatsoever (the nearest

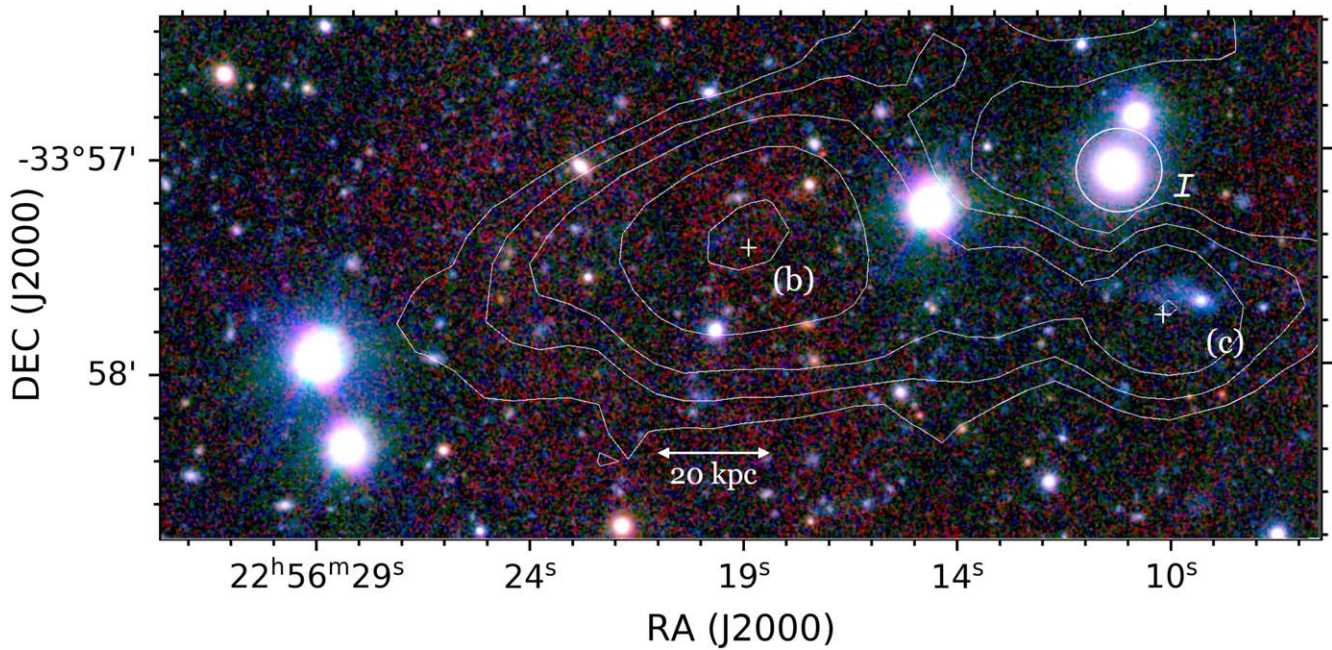


**Figure 6.** Central concentration of gas in the dark cloud chain shown in Figures 3(a) and (b). The image shows the KiDS  $g,r,i$  bands (blue, green, red), overlaid with contours of the H I column density: 3, 5, 8, 14, and  $23 \times 10^{19}$  atoms  $\text{cm}^{-2}$ . White crosses demark H I detections for Source (b) and Source (c). The closest Group-83 galaxy to the chain is labeled I. There are no clear optical associations with the densest gas in the entire region (Source (b)). However for Source (c) we do detect a small *blue* dwarf galaxy; see Figure 7 for a detailed view of Source (c).

GAMA galaxy is labeled V in Figure 1, a non-group member at the more distant redshift of 0.0324), which also implies this is a very dark patch of the cloud chain.

Source (b) is the massive concentration (see above for the discussion of the properties and  $M/L$  estimates.)

Potential Association: Source (c) is located directly west of the central mass (Source b) and  $55''$  due south of Group-83 member I (Figure 3 and Figure 6). It appears to be connected through a bridge of gas that extends  $\sim 2'$  ( $\sim 70$  kpc) from the cloud core (Figure 3(a)), implying a physical association with the main cloud core. Intriguingly, there is a faint optical source about  $13''$  to the west of the central location of the H I detection we label as (c); Figure 3(b). This is a plausible association, well within the HPBW of this H I map.

Moreover for Source (c), close inspection of the  $r$ -band image (see Figure 7) reveals that the optical source has a distorted *tail* that extends north-eastward toward the massive H I cloud (Source (b)). Might this be a gravitational tidal distortion coming from current or previous group interaction? Integrating a large ( $20''$  diameter) aperture to capture the core and tail emission, the resulting AB magnitude is  $19.51 \pm 0.01$ , corresponding to a flux density of  $57.0 \mu\text{Jy}$ . There is no optical GAMA redshift for this source, so we cannot be certain it is associated. The reason this source does not have a GAMA redshift is because in the original GAMA target catalogs, which are based on AUTO photometry of SDSS imaging, it was fainter than the 19.8 mag  $r$ -band selection limit. It does, however, have a GAMA DR4 photometric redshift because it was detected and extracted in the deeper photometric catalogs. The GAMA source is located at R.A., decl. (J2000deg) = 344.037096,  $-33.96165$ . For this source, the best photo- $z$  estimate is  $z_{\text{peak}} = 0.0357$  with a 68% confidence interval (0.024, 0.049), which is certainly consistent with this galaxy being a member of Group-83, or at least the  $z = 0.03$  filament.

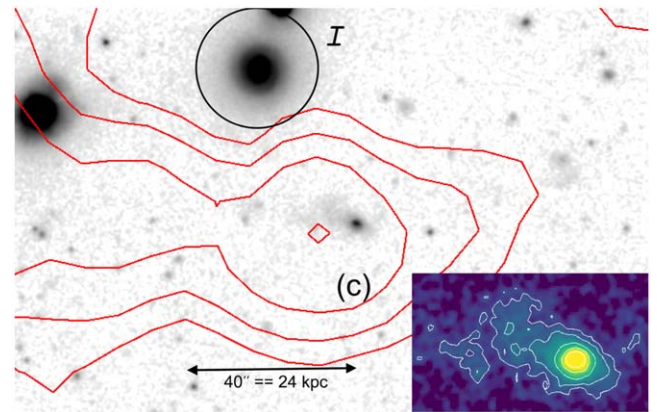


**Figure 7.** Close view of Source (c) with KiDS  $r$ -band imaging. As in the previous figures, the H I contours (red) indicate the gas distribution, with the (c) concentration in close proximity to the optical galaxy. Shown in the lower right is an inset image of a zoomed view of the optical source (with color transform *viridis*), located at (deg J2000) 344.03668-33.961783. The white contours, ranging from 25.8–22.5 mag  $\text{arcsec}^{-2}$ , delineate the low surface brightness *tidal tail* extending to the eastward toward the massive dark cloud core.

If we thus consider this to be an association, and adopt the distance of Source (c), the optical  $r$ -band luminosity would be  $10^{8.30} L_{\odot}$ . The corresponding H I mass for this source is  $10^{9.15} M_{\odot}$  (see Table 3), which would then imply an  $M_{\text{H I}}/L_r$  of  $\sim 8$ . This is a plausible ratio (although on the high side) for dwarf and star-forming galaxies (Staveley-Smith et al. 1992; Nalumsina et al. 2021), while also more extreme metal-poor dwarf examples have similarly high ratios (see, e.g., Filho et al. 2013). In addition, Source (c) is also clearly detected in the UV (Figure 3(d)), which strongly suggests active star formation. This is consistent with a tidal or a gravitational encounter, triggering recent star formation.

Other bands: At lower energies, the source is detected in the WISE near-IR (W1) image (Figure 3(c)), at coordinates[deg]

344.03632-33.96150. Emission at this wavelength implies an older stellar population is already in place. We can estimate the stellar mass using the prescription from Cluver et al. (2014); starting with the integrated  $W1$  magnitude,  $17.16 \pm 0.11$  ( $\sim 42 \mu\text{Jy}$ ), and assuming the distance to the cloud is 126 Mpc, the in-band luminosity is then  $10^{8.64} L_{\odot}$ . Adopting an  $M_{*}/L$  ratio of 0.4, appropriate to late-type galaxies, the implied stellar mass is then  $10^{8.2} M_{\odot}$ .

Hence, if this source is associated with the HI cloud, namely, Source (c), it is a dwarf galaxy that has recently been activated in star formation, likely from tidal forces, and which possesses older stellar populations anchoring the internal structure. The gas-to-stellar mass ratio ( $M_{\text{HI}}/M_{*}$ ) is  $\sim 3$ , which is well above the typical scaling relations seen for nearby galaxies, with ratios  $\leq 1$  (see, e.g., Nalumsa et al. 2021). We surmise either too much gas is attributed to this clump (since it is part of a larger complex, with a gas bridge to its massive neighbor), or the cloud is anomalously rich in neutral hydrogen.

Moving to the north side of the cloud complex, Source (d) is to the northwest of the massive cloud (b), and is directly  $1'$  north of Group-83 member I (note that both Source (c) and (d) are about equidistant north to south from Group-83 member I). This source also appears to be connected by a gas bridge to the larger complex; see Figures 3(a) and (b). In close proximity to the HI detection, we see a clear optical detection, roughly  $8''$  from the nominal HI centroid (i.e., within the beam of the radio measurements). There is no optical redshift for this source, so we cannot definitively associate it with the gas concentration. If we make the assumption that it is the host of the Source (d) gas emission, we can estimate its stellar mass using the WISE  $W1$  image, also well detected (Figure 3(c)). The source is seen in WISE at J2000 coordinate[deg] 344.04672-33.93435, and has an integrated  $W1$  magnitude (Vega) of  $15.31 \pm 0.31$  (0.23 mJy), and  $W1$ - $W2$  color of  $-0.03$  mag, and is undetected in the longward (ISM sensitive)  $W3$  and  $W4$  bands. These color properties imply an early-type, likely bulge-dominated, host galaxy. The estimated  $W1$  luminosity and stellar mass follows from assuming the distance (126 Mpc) to the cloud and the  $M/L$  color method of Cluver et al. (2014):  $10^{9.36 \pm 0.03} L_{\odot}$  and  $10^{9.1} M_{\odot}$ , respectively. Hence, if this source is associated with the cloud complex, then the computed stellar mass implies a dwarf spheroidal galaxy. This possible association seems less certain given the early-type colors of the optical/IR sources, which is more consistent with a gas-poor galaxy; nevertheless, it is a plausible association.

Moving to the last set of sources in the cloud complex: to the west of the massive gas core, Source (e) has no obvious large counterpart in the UV, the optical, or the infrared. But there is an faint blue-fuzzy source  $\sim 10''$  to the east, located at (J2000):  $344^{\circ}01206 - 33^{\circ}94493$ , which is worthy of follow-up. Similarly but on the opposite side of Source (e) to the west, there is diffuse emission that is well spread across  $20''$ - $30''$  in length. As best we can measure, the center of this diffuse structure is located at  $344^{\circ}0040, -33^{\circ}9458$ , and overall has a blue color implying active or recent star formation. It is plausible that this is a very low SB galaxy lurking near or within the HI cloud chain, or is a piece of a larger UDF galaxy system, and is worthy of follow-up deep imaging.

Source (f), located in the westernmost cloud which is closest to the Group-83 center (compact group of galaxies), seems to split a close pair of faint optical galaxies (Figure 3(b)).

Fortunately, these optical counterparts do have a redshift, but with a value of  $z \sim 0.16$ , i.e., they are well distant galaxies and hence clearly not associated with the HI complex.

Source (g), the final source of the gas chain is in the westernmost gas concentration. It has a more amorphous and diffuse morphology, less certain to be a discrete galaxy. There are no UV-optical-infrared sources in close proximity to its core. However, there is an early-type galaxy about  $30''$  to the SW of the core (see Figure 3(b), green circle near Source (g)). This source is identified as being in the filament and part of a galaxy pair ( $N = 2$  group). It has a redshift of  $z = 0.0272$  (versus 0.0294 for (g)), and hence is slightly in front of the cloud complex (115 versus 125 Mpc, assuming no peculiar motions). This relatively bright source ( $W1 = 13.38$  mag or 1.4 mJy), located at (deg J2000)  $343.9182; -33.9426$ , has WISE colors that indicate it is an early-type spheroid, with little or no star formation activity. Given the distance, velocity, and color mismatch, it is therefore unlikely to be associated with the HI dark cloud chain.

Finally, we note that Sources (d)-(g) appear to have a more filamentary structure, less discrete morphology, and are aligned toward the group's compact center, located  $9'$ - $10'$  ( $\sim 310$ - $350$  kpc) further to the west, with clouds (f) and (g) being connected by a gas bridge. This connection (f) and (g) shows the clearest velocity gradient of the whole complex (without having any clear association with a galaxy).

#### 4. Discussion

Three properties of the dark cloud chain are notable: (1) it is a dark HI complex, with a central source that is as massive as a gas-rich galaxy, but which shows no signs of previous or current star formation (yet one of the smaller concentrations may be associated with a tidal-distorted dwarf galaxy). Further to the absence of star formation activity, we note that radio continuum emission, at the position of the dark cloud chain, is not detected. On the other hand, the HI emission is detected in the single-dish HIPASS survey, with a peak surface brightness and integrated flux that is consistent with the MeerKAT measurements (see Appendix C), thus adding confidence of a real astrophysical detection. (2) It has hardly any kinematic structure along the radial direction, no larger than about  $110 \text{ km s}^{-1}$ , and with little evidence of rotation, and (3) it is located on the extreme edge of a large galaxy group: Group-83,  $N = 18$  members with  $z_{\text{for}} = 0.0289$  and a dynamical halo mass of  $10^{13.46} M_{\odot}$  and velocity dispersion of  $228.6 \text{ km s}^{-1}$ .

The cloud complex also appears *stretched* with multiple concentrations in the direction of the dense compact core of the Group-83. There is a noticeable absence of HI gas in the group, other than the cloud complex itself; it is a gas-poor group otherwise. What is the origin and nature of this massive cloud chain. Is the gas accreting into the group, perhaps merging from smaller clouds and now just entering the outer boundary, or might it be the ripped-apart detritus from an earlier tidal event between gas-rich massive galaxies in the group? That would require a very massive cast-off, from hosts that are not readily apparent in the region or even the filament itself. If this cloud is not self-supporting, how can it persist against tidal and photodisruption? We do not have enough information at this time to fully address these compelling questions.

As reviewed in Section 1, these types of dark HI clouds are quite rare, and massive ones ( $> 10^9 M_{\odot}$ ) are rarer still. Here, we have a complex that has a discrete source as massive as

$10^{9.7} M_{\odot}$ , and if we combine the gas for all seven sources the aggregate mass is  $10^{10} M_{\odot}$ , a rather large amount of neutral hydrogen floating at the edge of a sizable galaxy group (with a compact core) that is 3.5 orders of magnitude more massive (in total) than the gas cloud complex itself. Where did this neutral hydrogen come from, where is it going, and why is it not forming stars?

Notable examples of massive HI associations are the Leo Ring (Schneider et al. 1983; Schneider 1985; Schneider et al. 1986; Schneider 1989; Stierwalt et al. 2009), with a recently studied analog AGC 203001 (Bait et al. 2020), HI 1225+01 (Giovanelli & Haynes 1989), Hanny’s Voorwerp (Lintott et al. 2009; Józsa et al. 2009; Keel et al. 2012), HCG 44 (Serra et al. 2013; Hess et al. 2017), and AGC 229101 (Leisman et al. 2021).

The Leo Ring is an HI ring with a diameter of 200 kpc and a total mass of  $10^{9.3} M_{\odot}$  in the M96 galaxy group, long thought to lack a stellar counterpart (Schneider et al. 1986). As with the dark cloud chain, the ring forms a coherent, diffuse envelope around several concentrations. More recently it has been shown that the Leo Ring contains faint emission in the UV (Thilker et al. 2009), and/or has dust emission (Bot et al. 2009), and/or emission in the optical (Michel-Dansac et al. 2010) in a low number of concentrated HI clumps. Additionally, the metallicity measured along two sightlines is estimated to be at  $1/10 Z_{\odot}$ , showing that the Leo Ring, if of primordial origin, has to be enriched by the ISM of surrounding galaxies and—if tidal—must stem from a low-metallicity object, making the disruption of an LSB galaxy a potential scenario for its formation (Rosenberg et al. 2014). This would, however, also result in the additional detection of a stellar component. Stars have been associated to knots in the ring (Michel-Dansac et al. 2010), but a search for more massive dwarf objects has borne ambiguous results so far (Stierwalt et al. 2009, see also Bait et al. 2020 for a discussion).

As an association of HI concentrations, the Leo Ring can be compared to the whole dark cloud chain or associations therein, rather than just one of its constituents. The dark cloud chain differs from the Leo Ring in a number of important ways. First, we identify a star-forming dwarf galaxy as potentially being associated to Source (c). Second, the total mass of the dark cloud chain with ( $10^{10.0} M_{\odot}$ ) is 5 times larger than the Leo Ring, and third, it is twice as extended (as the diameter of the Leo Ring equals half the linear size of the dark cloud chain). At first sight, one might interpret the appearance of the dark chain as a chain with two linear parts, (a)–(c) and (d)–(g) rather than a ring. On the other hand, considering the configuration of Sources (b)–(e) and the surrounding HI only, with a diameter of  $3''6 \equiv 125$  kpc between Sources (b) and (e), the impression arises that the inner part of the observed HI might form a ring with a projected major axis between Source (b) and Source (e). Sources (a), (f), and (g) would then constitute extensions, which are also observed for the Leo Ring (toward M96, see Schneider 1985). With the early-type Group-83 galaxy I, the dark cloud chain (or ring) might also have a central object.

However, unlike the Leo Ring, the dark cloud chain would barely rotate, as the velocity difference between (b) and (e) with  $\sim 20$  km s $^{-1}$  lies below the nominal velocity resolution of our data. Correcting for an inclination of minimally  $\sim 30^{\circ}$  (by inspection) results in a rotational amplitude of  $\lesssim 20$  km s $^{-1}$ . The Leo Ring has a rotational amplitude of  $\sim 250$  km s $^{-1}$  (Schneider 1985), which differentiates it from the cloud chain.

Moreover, the systemic velocity of Group-83 galaxy I differs from that of the dark cloud chain by  $\sim 500$  km s $^{-1}$ , making an association somewhat tenuous. Given the limited kinematic information of our MeerKAT observations, we cannot rule out a ring-type gas distribution, perhaps associated with a galaxy-galaxy collision (see below), yet the properties of the cloud and the local environment do seem to indicate a different framework in place.

Consider a similar ring-like object, a massive ring around the galaxy AGC 230001 with a diameter of 115 kpc, an HI mass of  $M_{\text{HI}} = 10^{9.4} M_{\odot}$ , and with little stellar mass has been found by Bait et al. (2020). Interpreting the velocity gradient along the AGC 230001 ring ( $W_{20} = 100$  km s $^{-1}$ ) as rotation, and assuming an inclination of  $i \sim 60^{\circ}$  the estimated rotational speed of  $\sim 60$  km s $^{-1}$  is still significant, clearly larger than the case for the dark cloud chain. As with the Leo Ring, it too is kinematically and morphologically associated to a (quenched) massive galaxy (AGC 230001), which has the same systemic velocity as the ring.

It might hence appear that the Leo Ring or AGC 230001 differs from the dark cloud chain. Nevertheless, at least attempts to explain their nature might be applicable to the dark cloud chain. Michel-Dansac et al. (2010) simulate a head-on collision between two gas-rich spiral galaxies, resulting in a ring-like structure of extended debris, which the authors compare to the Leo Ring. Candidates for galaxies in this type of scenario in the case of the dark cloud chain could be Group-83 galaxies I and II, both of which are gas-poor and passive in star formation. The Leo Ring and AGC 230001 will remain objects for comparison in the future as the data on our newly discovered object accumulates.

Continuing our review of remarkable dark HI systems, HI 1225+01 is an enigmatic system at the edge of the Virgo Cluster, consisting of a giant HI cloud with two massive concentrations, a NE concentration with  $M_{\text{HI}} = 10^{9.4} M_{\odot}$ , and a SW concentration with a mass of  $M_{\text{HI}} = 10^9 M_{\odot}$ , respectively, the more massive of which harbors a diffuse star-forming dwarf galaxy, and for the less massive of which no stellar counterpart has been detected (Djorgovski 1990; McMahon et al. 1990; Giovanelli et al. 1991). Matsuoka et al. (2012) showed that the NE cloud has ongoing star formation, while the SW concentration does not contain stars to a limit of  $R_{\text{AB}} > 28$  mag arcsec $^{-2}$  over an area of  $10''$ .

The HI radius of HI 1225+01 compared to its optical extent would be outstanding among dwarf galaxies (Hoffman et al. 1996). The two clouds are embedded in a common envelope of HI. This system might be the most similar to the dark cloud chain, although it has half the mass and half the extent ( $\sim 200$  kpc) of the dark cloud chain. It shows a shallow velocity gradient of 44 km s $^{-1}$  between the two concentrations, while the spectral width of the concentrations itself is  $\sim 45$  km s $^{-1}$  for the NE cloud and  $\sim 25$  km s $^{-1}$  for the SW cloud (Giovanelli et al. 1991). Similar velocity gradients in the dark cloud chain would be consistent with our observations with their coarse velocity resolution. Again, whether the dark cloud chain and its largest concentration, Source (b), might be the more massive sister system to HI 1225+01 can only be confirmed in future studies, in particular, high-resolution HI observations.

Hanny’s Voorwerp is a large ionization nebula in the surroundings of the disk galaxy IC 2497, separated by  $\sim 20$  kpc (Lintott et al. 2009). Józsa et al. (2009) could show that the ionization region is part of a massive HI cloud with

$M_{\text{HI}} = 10^{9.7} M_{\odot}$ , which itself has an additional companion some 100 kpc to the west of IC 2497 with a mass of  $M_{\text{HI}} = 10^{9.5} M_{\odot}$ , again potentially connected by a gas bridge. The galaxy itself was not found to contain significant amounts of HI. While the literature largely concentrates on the origin of the ionization nebula as a light echo of a ceased quasar at the center of IC 2497, the origin of this extremely massive extragalactic cloud system has not been studied in detail. Keel et al. (2012) showed that the ionization nebula shows star formation, probably induced by a mild shock from an outflow of IC 2497, but no additional stellar component to the rest of the cloud. While the system is hence comparable to the dark cloud chain in mass and in extent, it is insofar different as an interaction partner, IC 2497 is clearly present. Should the cloud complex be the result of a tidal interaction, though, the whereabouts of the interaction partner would not be known, given the lack of follow-up studies.

Hickson Compact Group HCG 44 might provide a clue to the potential origin of massive, seemingly isolated clouds. As first discovered by Serra et al. (2013), HGC 44 shows a very elongated HI tail, which could be the result of intragroup gas stripping or a tidal interaction of the group with the spiral galaxy NGC 3162 at a distance of 650 kpc. No stars were found to a limiting  $g$ -band surface brightness of  $28.5 \text{ mag arcsec}^{-2}$ . Hess et al. (2017) demonstrated that the extent of the tail is 450 kpc with a total mass of  $10^9 M_{\odot}$ . While this is a factor of 10 less than the dark cloud chain, it is apparently possible to generate extremely massive, extremely widespread debris in galaxy interactions. In the case of the dark cloud chain, should it be the result of tidal origin, we might venture an age estimate by assuming an encounter at the center of the central group, at a distance of 400 kpc, assuming an upper limit of twice the dispersion of the group ( $457 \text{ km s}^{-1}$ ) as its velocity, resulting in a lower limit of 700 Myr.

Might there be an extreme low surface brightness galaxy, akin to UDGs, just beyond the sensitivity of our optical and infrared images? UDGs, with a central surface brightness  $>24 \text{ mag arcsec}^{-2}$  (AB) (and  $r_{\text{eff}} > 1.5 \text{ kpc}$ ) are found in galaxy groups and cluster environments at the distance of Group-83 and the dark cloud chain (see, e.g., van Dokkum et al. 2015; van der Burg et al. 2017; Zaritsky et al. 2019); moreover, KiDS imaging has been successfully deployed to find such objects down to  $26 \text{ mag arcsec}^{-2}$  (Karademir et al. 2021). For a group with mass the size of Group-83, we can expect to find a few UDGs ( $\sim 4$ – $5$ ) based on number counts versus group  $M_{200}$  masses (see Figure 3 in van der Burg et al. 2017). Our  $r$ -band image is sensitive enough to detect UDGs down to  $<26 \text{ mag arcsec}^{-2}$  or so, which is more than adequate to detect prototypical UDGs. And yet inspection of the central region of the dark cloud chain does not reveal any such faint emission, nor with additional binning and smoothing to enhance the signal-to-noise ratio. Either the stellar content is even lower mass and fainter than these limits, or the dark cloud is not forming, nor ever has, formed stars—this seems unlikely if the Source (c) association with a dwarf galaxy is real, and the diffuse blue-fuzzy source close to Source (e) is also associated.

A recent dark cloud discovery (Leisman et al. 2021) of a similarly massive neutral hydrogen cloud has identified a dwarf mass stellar counterpart at a surface brightness that is 0.5–1.0 mag below our own  $r$ -band limit, which emphasizes the possibility of an older stellar population at such extreme

surface brightnesses, which would be in line with our  $M_{\text{HI}}/M_{*}$  estimate being greater than 1000.

A final consideration, the dark matter content of the cloud. If the gas cloud is potentially relaxed, would it require dark matter to stabilize? Using the line width  $w_{20} = 139 \text{ km}^{-1}$  and assuming a Gaussian line profile, we derive a dispersion  $\sigma_z = 39 \text{ km s}^{-1}$ . Assuming a diameter of  $2R = 50 \text{ kpc}$  and a constant density distribution, the virial mass  $\frac{M_{\text{vir}}}{M_{\odot}} = 2.325 \times 10^5 \times 5 \left( \frac{\sigma_z}{\text{km s}^{-1}} \right)^2 \times \frac{R}{\text{kpc}}$  of the central concentration is  $4.4 \times 10^{10} M_{\odot} = 10^{10.6} M_{\odot}$ . With the assumption of an isothermal  $\left( \frac{1}{r} \right)$  mass profile  $\left( \frac{M_{\text{vir}}}{M_{\odot}} = 2.325 \times 10^5 \times 2 \left( \frac{\sigma_z}{\text{km s}^{-1}} \right)^2 \times \frac{R}{\text{kpc}} \right)$ , this reduces to  $1.8 \times 10^{10} M_{\odot} = 10^{10.2} M_{\odot}$  (see, e.g., Hoffman et al. 1996). Assuming a full rotational support, a lower limit (assuming an inclination of  $90^\circ$ ) to the dynamical mass  $\left( \frac{M_{\text{dyn}}}{M_{\odot}} = 2.325 \times 10^5 \times \left( \frac{0.5 w_{20}}{\text{km s}^{-1}} \right)^2 \times \frac{R}{\text{kpc}} \right)$  is  $2.8 \times 10^{10} M_{\odot} = 10^{10.4} M_{\odot}$ . This means that Source (b) with an HI mass of  $M_{\text{HI}} = 10^{9.7} M_{\odot}$ , should it be a stable structure (whether rotationally or pressure supported), likely requires some amount of dark matter to be long lived, with a total-to-luminous matter ratio of  $2.6 > \frac{M_{\text{tot}}}{M_{\text{lum}}}$  (scaling the HI mass by a factor of 1.4 to account for helium). Without any rotation this is less than would be typical for a galaxy. Notice that no attempt has been made to correct the line widths for the effect of instrumental broadening, as the filter function of the MeerKAT bandpass is close to a rectangle (nearly no spill from one channel into the neighboring channels). A slight broadening would bias our results to a higher total mass, underlining the conclusion that Source (b) might have a deficiency of dark matter as compared to a galaxy. At this stage it is, however, not known whether the cloud complex has any gravitationally bound concentrations, such that it is also possible that their kinematics and mass distribution are not obviously connected. Moreover, given the implied dynamical or halo mass we would expect a dwarf galaxy of  $M_{*} \geq 10^9 M_{\odot}$ , which is not the case.

The cloud chain remains an enigma, with many open questions; it will take further investigation to address these issues, starting with higher velocity resolution observations to better understand the kinematics of the complex, and deeper optical imaging to detect or rule out an extreme LSB galaxy. Notwithstanding the total absence of past star formation, a reasonable hypothesis to test is the possibility of a large disk galaxy being viewed relatively face-on, with smaller cloudlets (accretion?) associated with the disk and with similar kinematics in the plane of the sky.

To shed more light on the nature of the cloud complex and the enigmatic brightest concentration, we will pursue full 32K observations using MeerKAT. Moreover, Cluver et al. (in preparation) will fully address the properties of the galaxies inhabiting the greater filament that houses the chain, including the star formation and stellar mass properties of the larger group, to help understand the environment in which the dark cloud chain has been evolving.

## 5. Summary

The MeerKAT Habitat of Galaxies Survey (MeerHOGS) was created to map local large-scale structures to investigate the gas-to-star formation processes, central to galaxy evolution

studies. Another purpose of MeerHOGS was to test preliminary (early development) of HI pipelines for the MeerKAT radio telescope. A prominent filament in the GAMA G23 region was targeted, covering  $\sim 7 \text{ deg}^2$  and a redshift range from 0.026–0.034 (7800–10,200  $\text{km s}^{-1}$  in cz).

We detected over 60 sources in HI, spread throughout the filament ranging in HI gas mass from  $10^{8.27}$ – $10^{9.92} M_{\odot}$ . But in the course of comparing the HI sources to our GAMA and 2dFGRS redshift catalogs, we identified a *chain* of HI emission with a total HI mass of  $10^{10} M_{\odot}$  that did not have any counterparts. Further investigation, using deep ultraviolet, optical, and infrared imaging (GALEX, KiDS, and WISE, respectively), reveal this gas chain to be extremely dark: there is no emission from stars or star formation in proximity to the dark chain, most notably the massive central source, with  $10^{9.7} M_{\odot}$  in neutral hydrogen within 50 kpc diameter, implying an extreme gas mass-to-light ratio. One smaller source located  $\sim 70$  kpc to the west of the cloud core, however, may have a faint optical counterpart which has dwarf (low-mass) properties and is tidally disturbed (assuming it is associated and hence at the distance of the cloud complex); this is likely given the photometric redshift consistent with being at the distance of the cloud or large-scale filament.

In general, the cloud complex appears to be seven HI peak concentrations, extending  $\sim 400$  kpc from east to west (and possibly larger, smaller clouds are seen further afield yet aligned). The source has been validated to be real and not an artifact, and moreover, it is detected in HIPASS with a peak surface brightness and integrated flux that are wholly consistent with the MeerKAT measurements.

The size and mass of the central concentration is expected for a large, gas-rich, rotating galaxy, and yet, without any apparent UV, optical, or infrared counterpart to confirm such expectations. Adding to the mystery, this central concentration and indeed the entire chain complex has very little kinematic structure,  $< 200 \text{ km s}^{-1}$ , making it difficult to identify any cloud rotation to definitively identify a discrete structure (i.e., a galaxy). The central mass concentration, requires some amount of dark matter should it be a stable structure.

The HI complex, which appears to be interconnected by a tenuous *chain* of HI, is within or at the edge of a large galaxy group, whose velocity dispersion is  $228.6 \text{ km s}^{-1}$  and with a corresponding dynamical mass of  $10^{13.5} M_{\odot}$ . It is located some  $\sim 400$  kpc in projection from the group center, a gas-poor compact group of early-type galaxies. Indeed, there does not seem to be any HI emission in the vicinity of the cloud complex, a relatively gas-poor region except for the complex reported here. Its chain morphology suggests an origin and evolution that is connected to an interaction within the galaxy group, in which case we estimate an upper limit to its age of 700 Myr. Comparing the dark cloud *chain* to dark HI clouds in the literature, it may be a larger version of HI 1225+01, but further observations are required, notably at higher spectral resolutions, to decode the nature of this enigmatic HI gas cloud complex.

The fact that interferometric MeerKAT was able to detect and resolve (unlike HIPASS) this extraordinary gas complex, underscores the power of MeerKAT to survey large regions, and the importance of the SKA paradigm to raise HI astronomy to the next level.

We thank Steve Schneider for a thorough review of this paper, with a number of helpful suggestions that have been implemented. We thank Thijs van der Hulst, Danielle Lucero, and John Hibbard for enlightening discussions. M.C. is a recipient of an Australian Research Council Future Fellowship (project No. FT170100273) funded by the Australian Government. T.H.J. acknowledge support from the National Research Foundation (South Africa).

The MeerKAT telescope is operated by the South African Radio Astronomy Observatory, which is a facility of the National Research Foundation, an agency of the Department of Science and Innovation.

Part of the data published here have been reduced using the CARACal pipeline, partially supported by ERC Starting grant No. 679629 “FORNAX”, MAECI grant No. ZA18GR02, DST-NRF grant No. 113121 as part of the ISARP Joint Research Scheme, and BMBF project 05A17PC2 for D-MeerKAT. Information about CARACal can be obtained online at <https://caracal.readthedocs.io>.

This publication makes use of data products from the Wide-field Infrared Survey Explorer, WISE, which is a joint project of the University of California, Los Angeles, and the Jet Propulsion Laboratory/California Institute of Technology, funded by the National Aeronautics and Space Administration.

GAMA is a joint European-Australasian project based around a spectroscopic campaign using the Anglo-Australian Telescope. The GAMA input catalog is based on data taken from the Sloan Digital Sky Survey and the UKIRT Infrared Deep Sky Survey. Complementary imaging of the GAMA regions is being obtained by a number of independent survey programs including GALEX MIS, VST KIDS, VISTA VIKING, WISE, Herschel-ATLAS, GMRT, and ASKAP providing UV to radio coverage. GAMA is funded by the STFC (UK), the ARC (Australia), the AAO, and the participating institutions. The GAMA website is located at <http://www.gama-survey.org/>. Based on observations made with ESO Telescopes at the La Silla Paranal Observatory under programme ID 177.A-3016.

*Software:* CARACal (Józsa et al. 2020), equolver (Józsa & Perkins 2021), SoFiA (Serra et al. 2015), Stimela (Makhathini 2018), AOFlagger (Offringa 2010), CUBICAL (Kenyon et al. 2018), WSClean (Offringa et al. 2014), iDaVIE (Jarrett et al. 2021).

## Appendix A

### MeerHOGS Survey Layout and Observational Parameters

#### A.1. MeerHOGS

Different to traditional blind surveys, MeerHOGS pointings are informed by the distribution of galaxies in a particular redshift range, thus optimized to detect galaxies residing within large-scale environments (see Cluver et al. in preparation for further details). The current study is based on a pilot survey, the effective area is closer to  $\sim 7 \text{ deg}^2$ , achieving the target HI sensitivity of 0.5 mJy over 209 kHz. A study of the 1.4 GHz continuum sources from MeerHOGS data was carried out by Yao et al. (submitted).

Illustrated in Figure 8, we positioned 20 pointings along the filament, and a further five pointings in the area of the dense galaxy group. The total integration time for each pointing was  $\sim 30$  minutes. Due to the overlap between the pointings, this corresponds to a co-added equivalent integration time of  $\sim 2$  hr

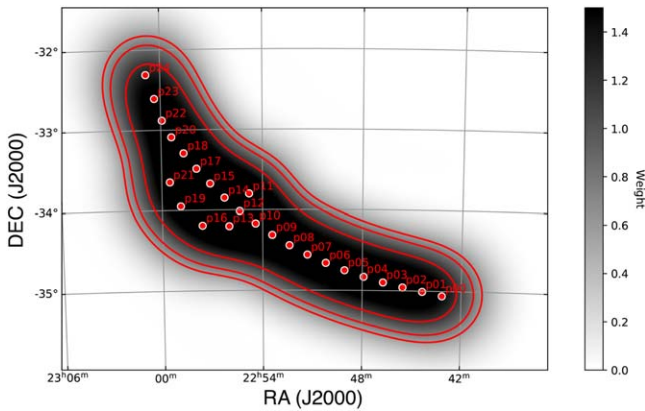


**Figure 8.** Observation footprint of the MeerHOGS field. The red points are the MeerKAT beam centers, with a total of 25 pointings. The combination of the ( $\sim$ Gaussian) beams creates the footprint, where the grayscale shows the accumulated coverage (weight), with the highest coverage ( $\sim$ 2 hr) in the central region, and the equivalent of 1 hr toward the edge (second contour).

at the center of the target structure and an equivalent integration time of approximately an hour along the filament (second contour in Figure 8).

### A.2. MeerKAT Observations

The MeerHOGS observations took place in four epochs in the second half of 2019 May, with a duration of 4–4.5 hr per observing run. The data were observed using the MeerKAT SCARAB Correlator in 4K mode. The total bandwidth was  $\sim$ 800 MHz, with 4096 channels of width 209 kHz, corresponding to  $45.4 \text{ km s}^{-1}$  at  $z \sim 0.02962$ . These observations were part of the MeerKAT Early Science program, which used a simpler 4K correlator. In the future, the full 32K channel mode will be available to significantly improve the velocity resolution.

In each observing run, each pointing was visited with an on-source integration time of 15 minutes. Between the target observations the gain calibrator J2302-3718 was visited for 2 minutes and the bandpass–and flux calibrator PKS 1934-63 was observed three times for 10 minutes in each observing epoch. The total observing time was 16.5 hr, with 13.2 hr being spent on-source to create the mosaic in Figure 8.

The achieved angular resolution (half-power beam width (HPBW)) in the continuum image after mosaicing is  $13''.5 \times 13''.5$ , which is uniform throughout the MeerHOGs region, while the angular resolution of the line data cube is  $34''.4 \times 34''.4$ ; further observation details given in Table 1, and detailed HI data reductions are below.

### A.3. Data Reduction: CARACal

Only part of the data were transferred from the SARAO archive for the HI data reductions, using the parallel-hand correlation products only. We used the frequency range from 1319.8–1517.1 MHz to both avoid RFI-dominated frequencies as well as to keep the data volume manageable. The primary data reduction was conducted using the platform-independent CARACAL pipeline<sup>20</sup> pipeline (Józsa et al. 2020). The data reduction took place on workstations typically using 36 computing cores and 300 GB of memory. CARACAL makes use of the STIMELA PYTHON framework, which combines a

large variety of available data reduction software through containerization and a common PYTHON interface (Makhathini 2018). Unless otherwise stated, all steps described in the following were made from within the pipeline and hence the interface. We performed a standard interferometric data reduction including a self-calibration and subsequent mosaicing.

After downloading the data, a data set containing only the calibrator observations (PKS 1934-63 and J2302-3718) was constructed. For the resulting data set the first dump after each setup change (*quack-flagging*) and autocorrelations were flagged. The data were flagged for shadowing, then for RFI using AOFLAGGER (Offringa 2010). For the cross-calibration, only baselines above 150 m were used to perform a delay, bandpass, and gain calibration using the primary calibrator (PKS 1934-63). The gains were then transferred to the secondary calibrator (J2302-3718), to apply a combined gain and flux calibration, flag the data based on the solutions, then apply a combined gain and flux calibration again. The resulting calibration tables were transferred to the target observations. Following that, the target data were flagged again for setup changes, autocorrelations, shadowing, and RFI (using AOFLAGGER).

For the continuum imaging with WSCLEAN (Offringa et al. 2014) the target data were then binned by a factor of 16 to a channel resolution of 3.3 MHz and potential HI emission from the Milky Way (around 1420.4 MHz) was flagged in this data set. A Gaussian taper of  $7''$  was applied to the data while using a Robust weighting of  $-1$ . A region of  $3^\circ \times 3^\circ$  was imaged four times per pointing. For each imaging step, a CLEAN mask was generated using the SoFiA (Serra et al. 2015) source-finding software (using a threshold of 4, 4, 3.5, 3.5  $\sigma_{\text{rms}}$ , where  $\sigma_{\text{rms}}$  is the locally measured rms noise), to CLEAN the data with a CLEAN cutoff parameter of 0.2. The resulting CLEAN models were used for self-calibration with CUBICAL (Kenyon et al. 2018), correcting the phases only of the visibilities after the first two imaging iterations, and both the phase and the gains after the third imaging iteration. Using the EQUOLVER<sup>21</sup> package (at the time of the data reduction not yet implemented in CARACAL) the resulting continuum images were convolved to a common resolution of  $13''.5 \times 13''.5$ , where  $13''.5$  was the maximum HPBW in any direction. The resulting images had an rms noise of  $\sigma_{\text{rms}} = 18 \pm 2 \mu\text{Jy}$ . The images were finally mosaiced to the final continuum image, weighted by the (quadrature of) the primary beam, for which we used the prescription by Mauch et al. (2020).

### A.4. HI Data Cubes

Prior to line imaging, the gains obtained from the continuum self-calibration were applied to the original data with higher frequency resolution and the continuum models used in the self-calibration step were subtracted from the visibilities. For computational reasons, the data were then split into chunks of 20 MHz with an overlap of 5 MHz. For each chunk, the velocity reference frames were shifted from the (original) topocentric to heliocentric and an additional continuum subtraction was applied by fitting a 3rd order polynomial to the visibilities. The data were then imaged two times using a Robust weighting of 0 and a Gaussian taper of  $10''$ , to create data cubes with spatial dimensions of  $2 \times 2 \text{ deg}$ .

<sup>20</sup> <https://caracal.readthedocs.io>

<sup>21</sup> <https://pyproject.org/project/equolver/>

The data were CLEANED in a first iteration using WSCLEAN automasking (with a CLEAN threshold of  $10\sigma_{\text{rms}}$ ), to use again a CLEAN mask as calculated using the SoFiA source-finding software with a clip level of  $4\sigma_{\text{rms}}$  and a CLEAN cutoff level of  $0.5\sigma_{\text{rms}}$ . For each frequency range, the resulting cubes were convolved to the same resolution using EQUOLVER and then mosaiced, again weighted using the (quadrature of) the primary beam. To achieve a coherent data cube spanning the whole frequency range the data cubes were then combined again, using an interpolation in the overlapping frequency/velocity ranges. A final cube was thus created, dimensions  $5.7 \times 4.9$ , and 479 velocity channels.

#### A.5. Source Finding and Image-domain Continuum Subtraction

To identify HI sources and to improve the continuum subtraction, we once again employed SoFiA. For the source detection, the images were smoothed only in the spatial domain, and not the frequency domain, using 4 Gaussian filters with sizes 0, 3, 6, and 9 voxels. A mask was created by clipping the emission in each resulting convolved cube at a  $4\sigma_{\text{rms}}$ -level and combining the resulting mask. Subsequently, sources were identified as voxel-complexes (or “islands”) in the mask and a reliability calculation was applied to reject islands/sources whose statistical properties indicate a spurious detection (for details see Serra et al. 2015). Using our initial continuum subtraction in the visibility-domain, we did not exclude channels with emission, as with the large field of view of MeerKAT the number of channels removed from the calculation of the continuum data cube can become very large. However, this leads to a slight over-subtraction in channels around bright HI sources.

To mitigate any over-subtractions, we applied an additional continuum modeling to the data cube. A second-order Savitzky–Golay (Savitzky & Golay 1964) filter of the length of 51 channels was applied to the data cube, to create a residual continuum cube. Doing so, we interpolated (the continuum-) emission along the frequency axis at the positions of detected sources. The resulting continuum cube was subtracted from the original data cube, resulting in our final data cube, on which we ran SoFiA one final time. In the final run of SoFiA a source list was generated. The masks were inspected and those occasions identified where potential residual flux from strong continuum sources could mimic an HI source. Those were flagged and removed from the subsequent analysis. In total, 196 sources were detected. No strong continuum source was found in the vicinity of the constellation described in this paper and we did not notice any strong or even moderate signatures of RFI in the channel ranges discussed in this paper. We hence exclude the possibility that our observations reflect any type of measurement error.

### Appendix B VR Visualization of the Dark Cloud Chain

We deployed a new cutting edge visualization tool to investigate the dark cloud chain. Designed specifically to work with spectral-imaging cubes, *iDaVIE* (Immersive Data Visualization Interactive Explorer<sup>22</sup>) renders cubes in a room-scale 3D VR space, where the user can intuitively view and uniquely

interact with their data cube (Jarrett et al. 2021). The software suite is designed to work with FITS cubes and products from the SoFiA<sup>23</sup> (Serra et al. 2015) source-finding package, including the mask cubes and extracted source lists. *iDaVIE* also has the capability of uploading redshift catalogs, which we utilized to confirm cross matches between the HI and optical detections in the MeerHOGS region.

The dark cloud chain of HI emission is composed of several close peak concentrations, essentially blended into one object by the initial SoFiA extraction. We used *iDaVIE* to identify and separate the individual concentrations through a voxel editing process in which the mask was user edited in 3D, based on the spatial and kinematic distribution of the HI gas. The result of this human-pattern-recognition source deblending is shown in Figure 9, which shows a 3D rendering of the dark cloud chain as seen through the lens of the VR user. The HI emission is transformed to a color scale (here, we are showing two different examples). Although limited by the 2D flat page, these three views demonstrate the 3D structure of the dark cloud chain, characterized by dense gas concentrations stretched into a filamentary cloud complex, and with very little radial-velocity kinematics (2–3 channels) in the orthogonal direction. Finally, the edited mask is depicted with a transparent mesh grid, overlaid on the HI emission. Visually discerning which voxels need editing, the mask value is tagged to the identified source, which may then be used to extract the source and characterize it.

As first presented in Figure 3 and Table 2, the sources are labeled (a)–(g). The mask determines which voxels are used to compute the source characteristics (e.g., systemic velocity, spatial coordinates, integrated flux, etc). This method of dividing the chain into pieces based on the peak emission and extent is only an approximate deblending. It is inevitable that some emission will bleed over into neighboring sources; moreover, it is not clear if all the sources (or some combination thereof) are discrete or part of a larger diffuse and filamentary cloud. Nevertheless, the most massive of the group of seven, labeled (b), is both central and appears to be a discrete galaxy-sized object. The *iDaVIE* extraction of this central source is about as good as it can be done given the angular resolution ( $34''$  HPBW) and kinematic resolution ( $45 \text{ km s}^{-1}$ ) of the HI cube mosaic.

### Appendix C HIPASS Spectrum of the Dark Cloud Chain

HIPASS carried out a systematic HI survey of the southern hemisphere using the Parkes 64 m dish and multi-beam spectrometer (Barnes et al. 2001). The velocity range of the survey extends to  $12,700 \text{ km s}^{-1}$ , but rapidly decreases in completeness beyond  $\sim 4800 \text{ km s}^{-1}$ . Nevertheless, massive HI sources may be detected at more distant velocities; since the dark cloud is at  $v_{\text{opt}} \sim 8900 \text{ km s}^{-1}$ , we can at best expect a weak detection (the source does not exist in any cataloged HIPASS or HICAT listings).

We do, however, locate the source in region H187 of HIPASS. Using an improved data cube created for the HICAT (catalog) processing (Meyer et al. 2004; Zwaan et al. 2004), we extracted a spectrum centered on Source (b) (see Table 3), both its spatial and velocity intensity peaks and detected a source at its location and velocity. To improve the signal to noise, we

<sup>22</sup> <https://idavie.readthedocs.io/en/latest/> and Jarrett et al. (2021)

<sup>23</sup> <https://github.com/SoFiA-Admin/SoFiA>

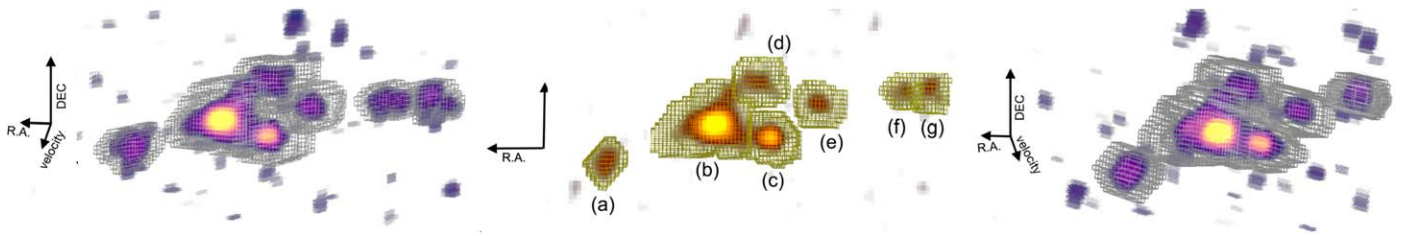


**Figure 9.** Three orientation views of the dark cloud chain using VR and the *iDAVIE* application. The 3D rendering is seen from the lens of the VR user. The H I gas distribution is shown with a color transform (*plasma, gist-heat, plasma* for the three views, respectively). The grid mesh demarcates voxels that are identified as having emission associated with the seven sources of the dark chain. The diagram shows that the chain is stretched along the east–west spatial plane, while relatively flat (only 2–3 channels) along the radial/velocity axis.

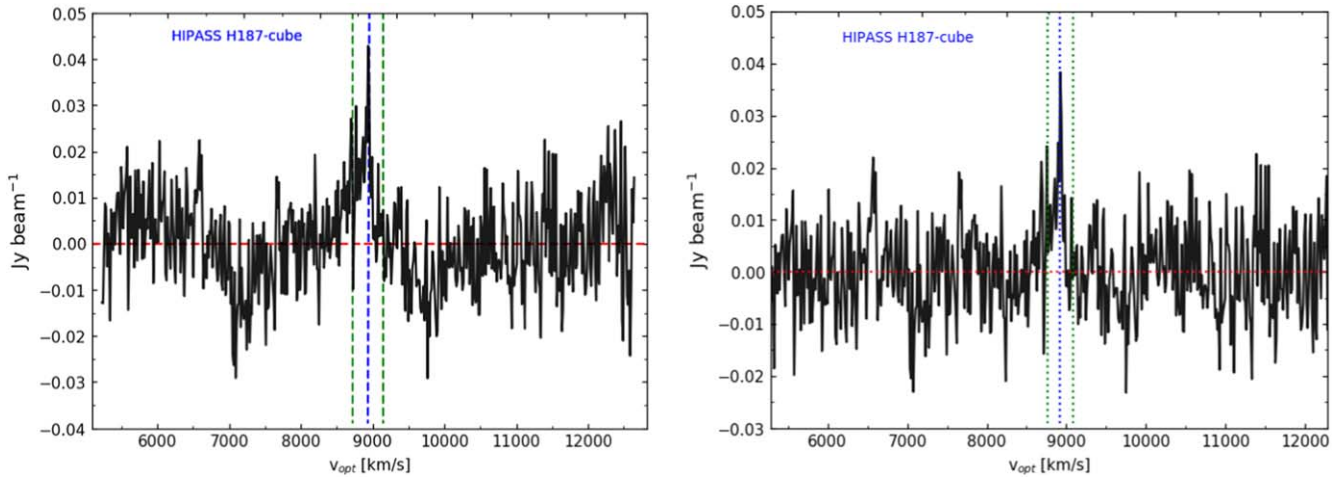


**Figure 10.** H I spectrum of the dark cloud chain as measured using the HIPASS cube H187 (wideband). The variation in the underlying continuum (left) has been fit and removed (right panel). The source is clearly detected at the spatial—R.A., decl. [deg J2000] = 344.080,  $-33.958$ —and velocity coordinates of the massive H I Source (b) (see blue vertical line at  $8886 \text{ km s}^{-1}$ ). The green lines demarcate the velocity limits for the spectrum integral.

averaged the H I surface brightness across  $\pm 3$  pixels in the spatial axis, or a region  $12'$  in width (the pixel scale of the cube is  $4'$ , while the spatial resolution or beam is about  $15.5'$ , and hence native pixels are highly correlated).

The source is clearly detected in the spectrum. There is, however, substantial variation in the background continuum levels due to the well-known *standing wave* ripple phenomenon inherent to single-dish radio telescopes (Briggs et al. 1997). Although there may be more optimal methods for removing said artifacts from the data (e.g., in the UV domain; see Popping & Braun 2008), we have simply used a cubic-spline fit to the spectrum to remove the first-order variations. We note that our goal here is to extract a coarse integrated flux of the source to compare with our MeerKAT measurements.

We experimented with fitting high-order polynomials and cubic splines with similar results. Fitting a spline3 to the underlying continuum (with the source itself masked from this fitting procedure to avoid overfitting and removing the source itself), the resulting spectrum is shown in Figure 10, before and after ripple correction; the channel width is  $13.2 \text{ km s}^{-1}$ . A zoomed velocity range is shown in the main text, centered on the cloud velocity, Figure 5. It is evident the large variations are removed for the most part, leaving a faint source detection at center. The channel-to-channel scatter in the background continuum (excluding the source) is  $8.95 \text{ mJy}$ , which we use to estimate the measurement signal to noise.

The peak emission is at a velocity of  $\sim 8886 \text{ km s}^{-1}$  with a flux density of  $0.038 \text{ Jy beam}^{-1}$  at the  $S/N = 4.2$  level. This peak corresponds to the peak velocity of Source (b) (see blue

line in Figure 10), which lends confidence to a real detection in the HIPASS cubes. Integrating the spectrum channels across  $\pm 150 \text{ km s}^{-1}$  (a wide enough range to capture all of the gas in system; see green lines in Figure 10), centered on the cloud systemic velocity (blue line), the integrated flux is  $2.9 \pm 0.6 \text{ Jy km s}^{-1}$ .

For the MeerKAT observations, we measure the integrated flux of Source (b) to be  $1.4 \text{ Jy km s}^{-1}$ , and of the entire complex to be  $\sim 2.8 \text{ Jy km s}^{-1}$ . Hence, the single-dish HIPASS results are consistent with the total flux of the dark cloud chain, given the large Parkes telescope beam ( $\sim 15.5'$ ) and excellent spatial coverage. These results lend confidence to a detection in the HIPASS survey, and conversely, to validation of the MeerKAT measurements.

## ORCID iDs

- G. I. G. Józsa <https://orcid.org/0000-0003-0608-6258>  
T. H. Jarrett <https://orcid.org/0000-0002-4939-734X>  
M. E. Cluver <https://orcid.org/0000-0002-9871-6490>  
O. I. Wong <https://orcid.org/0000-0003-4264-3509>  
O. Havenga <https://orcid.org/0000-0003-0995-0785>  
H. F. M. Yao <https://orcid.org/0000-0001-8459-4034>  
L. Marchetti <https://orcid.org/0000-0003-3948-7621>  
P. Kamphuis <https://orcid.org/0000-0002-5425-6074>  
S. V. White <https://orcid.org/0000-0002-2340-8303>  
V. Kilborn <https://orcid.org/0000-0003-3636-4474>  
B. W. Holwerda <https://orcid.org/0000-0002-4884-6756>  
S. Brough <https://orcid.org/0000-0002-9796-1363>  
K. A. Pimblet <https://orcid.org/0000-0002-3963-3919>

S. P. Driver  <https://orcid.org/0000-0001-9491-7327>  
 K. Kuijken  <https://orcid.org/0000-0002-3827-0175>

## References

- Allen, R. J., & Sullivan, W. T., III 1980, *A&A*, **84**, 181
- Appleton, P. N., Davies, R. D., & Stephenson, R. J. 1981, *MNRAS*, **195**, 327
- Auld, R., Minchin, R. F., Davies, J. I., et al. 2006, *MNRAS*, **371**, 1617
- Bait, O., Kurapati, S., Duc, P.-A., et al. 2020, *MNRAS*, **492**, 1
- Baldry, I. K., Robotham, A. S. G., Hill, D. T., et al. 2010, *MNRAS*, **404**, 86
- Baldry, I. K., Alpaslan, M., Bauer, A. E., et al. 2014, *MNRAS*, **441**, 2440
- Ball, C., Cannon, J. M., Leisman, L., et al. 2018, *AJ*, **155**, 65
- Banks, G. D., Disney, M. J., Knezek, P. M., et al. 1999, *ApJ*, **524**, 612
- Barkana, R., & Loeb, A. 1999, *ApJ*, **523**, 54
- Barnes, D. G., Staveley-Smith, L., Webster, R. L., & Walsh, W. 1997, *MNRAS*, **288**, 307
- Barnes, D. G., Staveley-Smith, L., de Blok, W. J. G., et al. 2001, *MNRAS*, **322**, 486
- Barnes, J. E., & Hernquist, L. 1996, *ApJ*, **471**, 115
- Bekki, K., Koribalski, B. S., & Kilborn, V. A. 2005a, *MNRAS*, **363**, L21
- Bekki, K., Koribalski, B. S., Ryder, S. D., & Couch, W. J. 2005b, *MNRAS*, **357**, L21
- Bellstedt, S., Driver, S. P., Robotham, A. S. G., et al. 2020, *MNRAS*, **496**, 3235
- Borthakur, S., Yun, M. S., & Verdes-Montenegro, L. 2010, *ApJ*, **710**, 385
- Bot, C., Helou, G., Latter, W. B., et al. 2009, *AJ*, **138**, 452
- Bothun, G. D., Impey, C. D., Malin, D. F., & Mould, J. R. 1987, *AJ*, **94**, 23
- Brammer, G. B., van Dokkum, P. G., & Coppi, P. 2008, *ApJ*, **686**, 1503
- Bravo-Alfaro, H., Cayatte, V., van Gorkom, J. H., & Balkowski, c. 2000, *AJ*, **119**, 580
- Bravo-Alfaro, H., Cayatte, V., van Gorkom, J. H., & Balkowski, c. 2001, *A&A*, **379**, 347
- Briggs, F. H. 1982, *ApJ*, **259**, 544
- Briggs, F. H. 1990, *AJ*, **100**, 999
- Briggs, F. H., Sorar, E., Kraan-Korteweg, R. C., & van Driel, W. 1997, *PASA*, **14**, 37
- Briggs, F. H., Wolfe, A. M., Krumm, N., & Salpeter, E. E. 1980, *ApJ*, **238**, 510
- Cannon, J. M., Martinkus, C. P., Leisman, L., et al. 2015, *AJ*, **149**, 72
- Cluver, M. E., Jarrett, T. H., Hopkins, A. M., et al. 2014, *ApJ*, **782**, 90
- Colless, M., Dalton, G., Maddox, S., et al. 2001, *MNRAS*, **328**, 1039
- Davies, J., Minchin, R., Sabatini, S., et al. 2004, *MNRAS*, **349**, 922
- Davies, R. D., & Wright, A. E. 1977, *MNRAS*, **180**, 71
- Díaz-Giménez, E., Mamon, G. A., Pacheco, M., Mendes de Oliveira, C., & Alonso, M. V. 2012, *MNRAS*, **426**, 296
- de Jong, J. T. A., Verdoes Kleijn, G. A., Erben, T., et al. 2017, *A&A*, **604**, A134
- Dickey, J. M. 1997, *AJ*, **113**, 1939
- Djorgovski, S. 1990, *AJ*, **99**, 31
- Doyle, M. T., Drinkwater, M. J., Rohde, D. J., et al. 2005, *MNRAS*, **361**, 34
- Driver, S. P., Hill, D. T., Kelvin, L. S., et al. 2011, *MNRAS*, **413**, 971
- Duc, P.-A., & Bournaud, F. 2008, *ApJ*, **673**, 787
- Efstathiou, G. 2000, *MNRAS*, **317**, 697
- English, J., Koribalski, B., Bland-Hawthorn, J., Freeman, K. C., & McCain, C. F. 2010, *AJ*, **139**, 102
- Filho, M. E., Winkel, B., Sánchez Almeida, J., et al. 2013, *A&A*, **558**, A18
- Fisher, J. R., & Tully, R. B. 1981a, *ApJS*, **47**, 139
- Fisher, J. R., & Tully, R. B. 1981b, *ApJL*, **243**, L23
- Flynn, C., Holmberg, J., Portinari, L., Fuchs, B., & Jahreiß, H. 2006, *MNRAS*, **372**, 1149
- Giovanelli, R., & Haynes, M. P. 1989, *ApJL*, **346**, L5
- Giovanelli, R., Williams, J. P., & Haynes, M. P. 1991, *AJ*, **101**, 1242
- Giovanelli, R., Haynes, M. P., Kent, B. R., et al. 2005, *AJ*, **130**, 2598
- Gnedin, N. Y., & Kravtsov, A. V. 2006, *ApJ*, **645**, 1054
- Hart, L., Davies, R. D., & Johnson, S. C. 1980, *MNRAS*, **191**, 269
- Haynes, M. P. 1981, *AJ*, **86**, 1126
- Haynes, M. P., Giovanelli, R., & Chincarini, G. L. 1984, *ARA&A*, **22**, 445
- Haynes, M. P., Giovanelli, R., & Roberts, M. S. 1979, *ApJ*, **229**, 83
- Haynes, M. P., & Roberts, M. S. 1979, *ApJ*, **227**, 767
- Henning, P. A. 1992, *ApJS*, **78**, 365
- Henning, P. A. 1995, *ApJ*, **450**, 578
- Hess, K. M., Cluver, M. E., Yahya, S., et al. 2017, *MNRAS*, **464**, 957
- Hibbard, J. E., & Mihos, J. C. 1995, *AJ*, **110**, 140
- Hibbard, J. E., van der Hulst, J. M., Barnes, J. E., & Rich, R. M. 2001a, *AJ*, **122**, 2969
- Hibbard, J. E., van Gorkom, J. H., Rupen, M. P., & Schiminovich, D. 2001b, 2001ASPC, **240**, 657
- Hindman, J. V., Kerr, F. J., & McGee, R. X. 1963a, *AuJPh*, **16**, 570
- Hindman, J. V., McGee, R. X., Carter, A. W. L., Holmes, E. C. J., & Beard, M. 1963b, *AuJPh*, **16**, 552
- Hoffman, G. L., Lu, N. Y., & Salpeter, E. E. 1992, *AJ*, **104**, 2086
- Hoffman, G. L., Lu, N. Y., Salpeter, E. E., & Connell, B. M. 1999, *AJ*, **117**, 811
- Hoffman, G. L., Salpeter, E. E., Farhat, B., et al. 1996, *ApJS*, **105**, 269
- Huchtmeier, W. K., & Richter, O.-G. 1982, *A&A*, **109**, 331
- Janowiecki, S., Leisman, L., Józsa, G., et al. 2015, *ApJ*, **801**, 96
- Jarrett, T. H., Masci, F., Tsai, C. W., et al. 2013, *AJ*, **145**, 6
- Jarrett, T. H., Comrie, A., Marchetti, L., et al. 2021, *A&C*, **37**, 100502
- Józsa, G. I. G., & Perkins, S. 2021, caracal-pipeline/equlver: Doing again, 0.0.11, Zenodo, doi: 10.5281/zenodo.5703072
- Józsa, G. I. G., White, S. V., Thorat, K., et al. 2020, in ASP Conf. Ser. 527, ADASS XXIX, ed. R. Pizzo, E. R. Deul, J. D. Mol et al. (San Francisco, CA: ASP), **635**
- Józsa, G. I. G., Garrett, M. A., Oosterloo, T. A., et al. 2009, *A&A*, **500**, L33
- Karachentsev, I. D., Makarov, D. I., Karachentseva, V. E., & Melnik, O. V. 2008, *AstL*, **34**, 832
- Karademir, G. S., Taylor, E. N., Blake, C., et al. 2021, *MNRAS*, **509**, 5467
- Kauffmann, G., White, S. D. M., & Guiderdoni, B. 1993, *MNRAS*, **264**, 201
- Keel, W. C., Lintott, C. J., Schawinski, K., et al. 2012, *AJ*, **144**, 66
- Kent, B. R. 2010, *ApJ*, **725**, 2333
- Kent, B. R., Giovanelli, R., Haynes, M. P., et al. 2007, *ApJL*, **665**, L15
- Kenyon, J. S., Smirnov, O. M., Grobler, T. L., & Perkins, S. J. 2018, *MNRAS*, **478**, 2399
- Kilborn, V. A., Forbes, D. A., Koribalski, B. S., Brough, S., & Kern, K. 2006, *MNRAS*, **371**, 739
- Kilborn, V. A., Koribalski, B. S., Forbes, D. A., Barnes, D. G., & Musgrave, R. C. 2005, *MNRAS*, **356**, 77
- Kilborn, V. A., Staveley-Smith, L., Marquarding, M., et al. 2000, *AJ*, **120**, 1342
- Klypin, A., Kravtsov, A. V., Valenzuela, O., & Prada, F. 1999, *ApJ*, **522**, 82
- Koribalski, B., & Dickey, J. M. 2004, *MNRAS*, **348**, 1255
- Koribalski, B., Gordon, S., & Jones, K. 2003, *MNRAS*, **339**, 1203
- Koribalski, B., & Manthey, E. 2005, *MNRAS*, **358**, 202
- Koribalski, B. S. 2004, in Proc. IAU Symp. 217, Recycling Intergalactic and Interstellar Matter, ed. P.-A. Duc, J. Braine, & E. Brinks (Cambridge: Cambridge Univ. Press), **34**
- Kovač, K., Oosterloo, T. A., & van der Hulst, J. M. 2009, *MNRAS*, **400**, 743
- Krumm, N., & Brosch, N. 1984, *AJ*, **89**, 1461
- Kuijken, K., Heymans, C., Dvornik, A., et al. 2019, *A&A*, **625**, A2
- Lang, R. H., Boyce, P. J., Kilborn, V. A., et al. 2003, *MNRAS*, **342**, 738
- Larson, R. B. 1974, *MNRAS*, **169**, 229
- Leisman, L., Haynes, M. P., Janowiecki, S., et al. 2017, *ApJ*, **842**, 133
- Leisman, L., Rhode, K. L., Ball, C., et al. 2021, *AJ*, **162**, 274
- Li, J. G., & Seaquist, E. R. 1994, *AJ*, **107**, 1953
- Lintott, C. J., Schawinski, K., Keel, W., et al. 2009, *MNRAS*, **399**, 129
- Liske, J., Baldry, I. K., Driver, S. P., et al. 2015, *MNRAS*, **452**, 2087
- Lo, K. Y., & Sargent, W. L. W. 1979, *ApJ*, **227**, 756
- Makhathini, S. 2018, PhD thesis, Rhodes Univ.
- Martin, D. C., Fanson, J., Schiminovich, D., et al. 2005, *ApJL*, **619**, L1
- Martin, N. F., de Jong, J. T. A., & Rix, H.-W. 2008, *ApJ*, **684**, 1075
- Mathewson, D. S., Cleary, M. N., & Murray, J. D. 1974, *ApJ*, **190**, 291
- Mathewson, D. S., Cleary, M. N., & Murray, J. D. 1975, *ApJL*, **195**, L97
- Matsuoka, Y., Ienaka, N., Oyabu, S., Wada, K., & Takino, S. 2012, *AJ*, **144**, 159
- Mauch, T., Cotton, W. D., Condon, J. J., et al. 2020, *ApJ*, **888**, 61
- McKay, N. P. F., Mundell, C. G., Brough, S., et al. 2004, *MNRAS*, **352**, 1121
- McMahon, P. M., van Gorkom, J. H., Richter, O.-G., & Ferguson, H. C. 1992, *AJ*, **103**, 399
- McMahon, R. G., Irwin, M. J., Giovanelli, R., et al. 1990, *ApJ*, **359**, 302
- Meyer, M. J., Zwaan, M. A., Webster, R. L., et al. 2004, *MNRAS*, **350**, 1195
- Michel-Dansac, L., Duc, P.-A., Bournaud, F., et al. 2010, *ApJ*, **717**, L143
- Minchin, R., Davies, J., Disney, M., et al. 2005, *ApJL*, **622**, L21
- Minchin, R., Davies, J., Disney, M., et al. 2007, *ApJ*, **670**, 1056
- Moore, B., Ghigna, S., Governato, F., et al. 1999, *ApJL*, **524**, L19
- Naluninsa, E., Elson, E. C., & Jarrett, T. H. 2021, *MNRAS*, **502**, 5711
- Offringa, A. R. 2010, AOfFlagger, Astrophysics Source Code Library, ascl:1010.017 <https://gitlab.com/aroffringa/aoflagger>
- Offringa, A. R., McKinley, B., & Hurley-Walker, N. 2014, *MNRAS*, **444**, 606
- Oosterloo, T. A., Heald, G. H., & de Blok, W. J. G. 2013, *A&A*, **555**, L7
- Pisano, D. J., Wakker, B. P., Wilcots, E. M., & Fabian, D. 2004, *AJ*, **127**, 199
- Popping, A., & Braun, R. 2008, *A&A*, **479**, 903
- Putman, M. E., Bureau, M., Mould, J. R., Staveley-Smith, L., & Freeman, K. C. 1998a, *AJ*, **115**, 2345

- Putman, M. E., Gibson, B. K., Staveley-Smith, L., et al. 1998b, *Natur*, **394**, 752
- Quinn, T., Katz, N., & Efstathiou, G. 1996, *MNRAS*, **278**, L49
- Rees, M. J. 1986, *MNRAS*, **218**, 25P
- Roberts, M. S. 1968, *ApJ*, **151**, 117
- Roberts, M. S. 1972, in Proc. IAU Symp. 44, External Galaxies and Quasi-Stellar Objects, ed. D. S. Evans, D. Wills, & B. J. Wills (Cambridge: Cambridge Univ. Press), 12
- Robotham, A. S. G., Norberg, P., Driver, S. P., et al. 2011, *MNRAS*, **416**, 2640
- Rosenberg, J. L., Haislmaier, K., Giroux, M. L., Keeney, B. A., & Schneider, S. E. 2014, *ApJ*, **790**, 64
- Rosenberg, J. L., & Schneider, S. E. 2000, *ApJS*, **130**, 177
- Ryder, S. D., Koribalski, B., Staveley-Smith, L., et al. 2001, *ApJ*, **555**, 232
- Sancisi, R., van Woerden, H., Davies, R. D., & Hart, L. 1984, *MNRAS*, **210**, 497
- Savitzky, A., & Golay, M. J. E. 1964, *AnaCh*, **36**, 1627
- Schneider, S. 1985, *ApJL*, **288**, L33
- Schneider, S. E. 1989, *ApJ*, **343**, 94
- Schneider, S. E., Helou, G., Salpeter, E. E., & Terzian, Y. 1983, *ApJL*, **273**, L1
- Schneider, S. E., Salpeter, E. E., & Terzian, Y. 1986, *AJ*, **91**, 13
- Schneider, S. E., Spitzak, J. G., & Rosenberg, J. L. 1998, *ApJL*, **507**, L9
- Serra, P., Westmeier, T., & Giese, N. 2015, *MNRAS*, **448**, 1922
- Serra, P., Koribalski, B., Duc, P.-A., et al. 2013, *MNRAS*, **428**, 370
- Shostak, G. S. 1974, *A&A*, **31**, 97
- Shostak, G. S. 1977, *A&A*, **54**, 919
- Sorar, E. 1994, PhD thesis, Univ. Pittsburgh
- Staveley-Smith, L., Davies, R. D., & Kinman, T. D. 1992, *MNRAS*, **258**, 334
- Stierwalt, S., Haynes, M. P., Giovanelli, R., et al. 2009, *AJ*, **138**, 338
- Taylor, C. L., Brinks, E., Grashuis, R. M., & Skillman, E. D. 1995, *ApJS*, **99**, 427
- Taylor, C. L., Brinks, E., Grashuis, R. M., & Skillman, E. D. 1996, *ApJS*, **102**, 189
- Taylor, E. N., & Webster, R. L. 2005, *ApJ*, **634**, 1067
- Taylor, R., Davies, J. I., Auld, R., & Minchin, R. F. 2012, *MNRAS*, **423**, 787
- Taylor, R., Davies, J. I., Auld, R., Minchin, R. F., & Smith, R. 2013, *MNRAS*, **428**, 459
- Taylor, R., Davies, J. I., Jáchym, P., et al. 2016, *MNRAS*, **461**, 3001
- Taylor, R., Davies, J. I., Jáchym, P., et al. 2017, *MNRAS*, **467**, 3648
- Taylor, R., Wünsch, R., & Palouš, J. 2018, *MNRAS*, **479**, 377
- Thilker, D. A., Donovan, J., Schiminovich, D., et al. 2009, *Natur*, **457**, 990
- Toomre, A., & Toomre, J. 1972, *ApJ*, **178**, 623
- van der Burg, R. F. J., Hoekstra, H., Muzzin, A., et al. 2017, *A&A*, **607**, A79
- van der Hulst, J. M. 1979a, *A&A*, **71**, 131
- van der Hulst, J. M. 1979b, *A&A*, **75**, 97
- van Dokkum, P. G., Abraham, R., Merritt, A., et al. 2015, *ApJ*, **798**, L45
- van Driel, W., O’Neil, K., Cayatte, V., et al. 2003, *A&A*, **399**, 433
- Verde, L., Oh, S. P., & Jimenez, R. 2002, *MNRAS*, **336**, 541
- Verdes-Montenegro, L., Yun, M. S., Williams, B. A., et al. 2001, *A&A*, **377**, 812
- Vollmer, B., Huchtmeier, W., & van Driel, W. 2005, *A&A*, **439**, 921
- Walter, F., Skillman, E. D., & Brinks, E. 2005, *ApJL*, **627**, L105
- Wannier, P., & Wrixon, G. T. 1972, *ApJL*, **173**, L119
- Weinberg, D. H., Szomoru, A., Guhathakurta, P., & van Gorkom, J. H. 1991, *ApJL*, **372**, L13
- Weliachew, L. 1969, *A&A*, **3**, 402
- Wolfinger, K., Kilborn, V. A., Koribalski, B. S., et al. 2013, *MNRAS*, **428**, 1790
- Wong, O. I., Webster, R. L., Kilborn, V. A., Waugh, M., & Staveley-Smith, L. 2009, *MNRAS*, **399**, 2264
- Wong, O. I., Stevens, A. R. H., For, B.-Q., et al. 2021, *MNRAS*, **507**, 2905
- Wright, E. L., Eisenhardt, P. R. M., Mainzer, A. K., et al. 2010, *AJ*, **140**, 1868
- Yun, M. S., Ho, P. T. P., & Lo, K. Y. 1994, *Natur*, **372**, 530
- Zaritsky, D., Donnerstein, R., Dey, A., et al. 2019, *ApJS*, **240**, 1
- Zwaan, M. A. 2001, *MNRAS*, **325**, 1142
- Zwaan, M. A., Briggs, F. H., Sprayberry, D., & Sorar, E. 1997, *ApJ*, **490**, 173
- Zwaan, M. A., Meyer, M. J., Webster, R. L., et al. 2004, *MNRAS*, **350**, 1210